

AzTEC millimetre survey of the COSMOS field – III. Source catalogue over 0.72 deg² and plausible boosting by large-scale structure

I. Aretxaga,^{1*} G. W. Wilson,² E. Aguilar,¹ S. Alberts,² K. S. Scott,³ N. Scoville,⁴ M. S. Yun,² J. Austermann,⁵ T. P. Downes,⁴ H. Ezawa,⁶ B. Hatsukade,⁷ D. H. Hughes,¹ R. Kawabe,⁷ K. Kohno,⁸ T. Oshima,⁷ T. A. Perera,⁹ Y. Tamura⁷ and M. Zeballos¹

¹*Instituto Nacional de Astrofísica, Óptica y Electrónica (INAOE), Aptdo. Postal 51 y 216, 72000 Puebla, Pue., Mexico*

²*Department of Astronomy, University of Massachusetts, Amherst, MA 01003, USA*

³*Department of Physics and Astronomy, University of Pennsylvania, Philadelphia, PA 19104, USA*

⁴*California Institute of Technology, Pasadena, CA 91125, USA*

⁵*Center for Astrophysics and Space Astronomy, University of Colorado, Boulder, CO 80309, USA*

⁶*ALMA Project Office, National Astronomical Observatory of Japan, 2-21-1 Osawa, Mitaka, Tokyo 181-8588, Japan*

⁷*Nobeyama Radio Observatory, Minamimaki, Minamisaku, Nagano 384-1305, Japan*

⁸*Institute of Astronomy, University of Tokyo, 2-21-1 Osawa, Mitaka, Tokyo 181-0015, Japan*

⁹*Department of Physics, Illinois Wesleyan University, Bloomington, IL 61701, USA*

Accepted 2011 April 28. Received 2011 April 26; in original form 2011 February 4

ABSTRACT

We present a 0.72 deg² contiguous 1.1-mm survey in the central area of the Cosmological Evolution Survey field carried out to a $1\sigma \approx 1.26$ mJy beam⁻¹ depth with the AzTEC camera mounted on the 10-m Atacama Submillimeter Telescope Experiment. We have uncovered 189 candidate sources at a signal-to-noise ratio (S/N) ≥ 3.5 , out of which 129, with S/N ≥ 4 , can be considered to have little chance of being spurious ($\lesssim 2$ per cent). We present the number counts derived with this survey, which show a significant excess of sources when compared to the number counts derived from the ~ 0.5 deg² area sampled at similar depths in the Submillimetre Common-User Bolometer Array (SCUBA) HALf Degree Extragalactic Survey (SHADES). They are, however, consistent with those derived from fields that were considered too small to characterize the overall blank-field population. We identify differences to be more significant in the $S_{1.1\text{mm}} \gtrsim 5$ mJy regime, and demonstrate that these excesses in number counts are related to the areas where galaxies at redshifts $z \lesssim 1.1$ are more densely clustered. The positions of optical–infrared galaxies in the redshift interval $0.6 \lesssim z \lesssim 0.75$ are the ones that show the strongest correlation with the positions of the 1.1-mm bright population ($S_{1.1\text{mm}} \gtrsim 5$ mJy), a result which does not depend exclusively on the presence of rich clusters within the survey sampled area. The most likely explanation for the observed excess in number counts at 1.1-mm is galaxy–galaxy and galaxy–group lensing at moderate amplification levels, which increases in amplitude as one samples larger and larger flux densities. This effect should also be detectable in other high-redshift populations.

Key words: surveys – galaxies: evolution – cosmology: miscellaneous – submillimetre: galaxies.

1 INTRODUCTION

The Cosmological Evolution Survey (COSMOS) 2 deg² field has been extensively targeted by a wide array of observations in order to probe the cosmic evolution of galaxies and the large-scale structure in which they are immersed (Scoville et al. 2007a). With a wealth of multiwavelength data spanning from X-rays to radio wavelengths,

and a core deep ultraviolet–optical–infrared (IR) survey with the highest resolution and sensitivity offered by space facilities (*HST*, *Spitzer*, *GALEX*), it provides a unique opportunity to study the relationships and interactions among galaxy populations selected at different wavelengths and across a wide array of environments in cosmic time.

A key contribution towards this knowledge comes from the far-IR (FIR) to millimetre (mm) wavelength regime, which has been shown to uncover ultraluminous violently star-forming galaxies at high redshifts ($z \gtrsim 2$) that would have gone undetected at

*E-mail: itziar@inaoe.mx

traditional optical–near-IR survey wavelengths due to their intrinsic high obscuration (Smail, Ivison & Blain 1997; Barger et al. 1998; Hughes et al. 1998). Named the (sub)mm galaxy population (SMG for short), this population has been linked to the formation of massive elliptical galaxies, with large luminosities $L \gtrsim 10^{13} L_{\odot}$, large star formation rates $\gtrsim 1000 M_{\odot} \text{ yr}^{-1}$, large reservoirs of gas $\gtrsim 10^{10} M_{\odot}$ and large dynamical $\gtrsim 10^{11} M_{\odot}$ and stellar masses $\gtrsim 10^{11} M_{\odot}$ (e.g. Greve et al. 2005; Dye et al. 2008; Tacconi et al. 2008).

Previous mm-wavelength surveys in COSMOS have covered areas which were significantly smaller than the full 2 deg^2 design survey, and the conclusions derived from the limited number of detected galaxies suffered from large field-to-field variations. COSBO (Bertoldi et al. 2007), a 1.2-mm survey carried out with the Max-Planck Millimeter Bolometer Array (MAMBO) mounted on the 30-m Institute for Radioastronomy at Millimeter Wavelengths telescope, detected 37 candidate sources at a signal-to-noise ratio (S/N) ≥ 3.5 in the central 0.09 deg^2 of COSMOS, which was mapped at a 1σ noise level of $\sim 1 \text{ mJy beam}^{-1}$. An adjacent 0.15 deg^2 field was imaged at 1.1 mm to a 1σ level of 1.2 to $1.4 \text{ mJy beam}^{-1}$ with the AzTEC instrument (Wilson et al. 2008a) mounted on the 15-m James Clerk Maxwell Telescope (JCMT), uncovering 50 candidate sources at an $S/N \geq 3.5$ (Scott et al. 2008). The combined area sampled by these two surveys amounts to only ~ 12 per cent of the total 1.4×1.4 COSMOS area.

Field-to-field variations in the derived overall properties of SMGs, such as number counts, redshift distributions or clustering, had already been reported in these kinds of smaller ($\lesssim 0.25 \text{ deg}^2$) fields and attributed both to variance due to the intrinsically small volume sampled by the surveys (e.g. Coppin et al. 2006; Aretxaga et al. 2007; Weiß et al. 2009; Austermann et al. 2010) and to the chance amplification by a foreground population of galaxies (Almaini et al. 2005; Austermann et al. 2009). Indeed, the environments traced by optical–IR galaxies in the COSMOS subfields were quite different: while the AzTEC survey focused on an area with an overdensity of optical–IR galaxies, COSBO sampled lower galaxy-density environments (see Fig. 1).

A more representative survey of the COSMOS field was thus necessary in order to investigate the culprits for these large variations and to characterize the global blank-field population at 1.1 mm. AzTEC alone has surveyed to date $\sim 2 \text{ deg}^2$ of the blank-field extragalactic sky at 1.1 mm, to $\approx 0.4\text{--}1.4 \text{ mJy beam}^{-1}$, coupled to 15- and 10-m telescopes with resolutions 18 and 30 arcsec, respectively (Perera et al. 2008; Scott et al. 2008, 2010; Austermann et al. 2009, 2010; Hatsukade et al. 2011; Ikarashi et al. 2011). The COSMOS survey of 0.72 deg^2 presented in this paper is the largest single-field extragalactic area mapped at 1.1 mm at these depths, and provides important constraints especially when compared to the Submillimetre Common-User Bolometer Array (SCUBA) Half Degree Extragalactic Survey (SHADES) fields mapped at 1.1 mm, of comparable extension and depth (Austermann et al. 2010).

Section 2 presents the AzTEC/Atacama Submillimeter Telescope Experiment (ASTE) observations in the COSMOS field. Section 3 details the data reduction processes employed to produce our 1.1-mm map. Section 4 characterizes the systematic properties of the map and derives the catalogue of source candidates from our observations. Section 5 compares the AzTEC source catalogue to other mm- and radio-wavelength catalogues in COSMOS. Section 6 presents the number counts over the 0.72 deg^2 area, which shows an excess over those of the 0.5 deg^2 SHADES field. Section 7 explores the origins of the excess in terms of cross-correlations with the

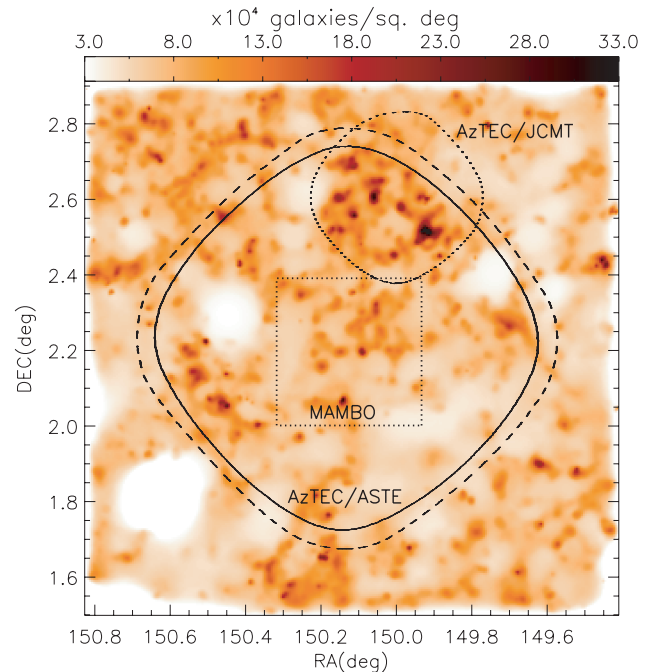


Figure 1. Representation of the optical–IR-selected galaxy-density map in the COSMOS field (Scoville et al. 2007b) and the uniform coverage areas of the mm surveys published to date: the MAMBO COSBO survey at 1.2 mm to a 1σ noise level of $\sim 1 \text{ mJy beam}^{-1}$ (Bertoldi et al. 2007) and the AzTEC/JCMT survey at 1.1 mm to a 1σ level of $1.2\text{--}1.4 \text{ mJy beam}^{-1}$ (Scott et al. 2008). The AzTEC/ASTE survey at 1.1 mm, presented in this paper, has an average 1σ noise level of $1.26 \text{ mJy beam}^{-1}$ within the 0.72 deg^2 uniform coverage area (solid line). Also represented is a concentric area that marks the 25 per cent coverage area of the survey, whose noise level increases towards the edges of the map.

optical–IR galaxy population, and Section 8 discusses the results and summarizes our conclusions.

2 OBSERVATIONS

We imaged a 2800 arcmin^2 field centred at right ascension RA (J2000.0) = $10^{\text{h}}00^{\text{m}}30^{\text{s}}.00$ and declination Dec. (J2000.0) = $2^{\circ}14'00''$ with AzTEC mounted on the 10-m ASTE (Ezawa et al. 2004, 2008), located at 4800 m in the Atacama Desert of Chile. The survey was carried out from 2008 October 20 to November 30 during excellent observing conditions with mean zenith opacity as reported by the ASTE monitor, $\tau_{220\text{GHz}} = 0.05$ and values of $\tau_{220\text{GHz}} < 0.06$ about 76 per cent of the time. ASTE was operated remotely with the N-COSMOS3 network system (Kamazaki et al. 2005) by observers deployed in San Pedro de Atacama (Chile), Mitaka and Nobeyama (Japan), Amherst (USA) and Tonantzintla (Mexico). A total of 112.6 h of on-bolometer time was devoted to this field, excluding calibration and pointing observations. The area was sampled in raster mode at $208 \text{ arcsec s}^{-1}$ along 52 arcmin stripes oriented in azimuth, spaced by 1 arcmin steps in elevation. Since the array orientation is fixed in azimuth and elevation, the scan angle in RA–Dec. continuously changes due to sky rotation, providing excellent cross-linking in the final combined image. A total of 203 raster scan maps were acquired in COSMOS during the 2008 observing season, each taking 33 min of observation in a single passage through the scanning area. Out of the 144 nominal bolometers of AzTEC, 117 were operative during this season.

Pointing observations were acquired every half an hour to an hour, sandwiching every one to two COSMOS raster maps, depending on observing conditions. The bright QSO 1055+018, $S_{1.1\text{mm}} \sim 2\text{Jy}$, was used to measure shifts from the standard ASTE pointing model. We acquired $\sim 4 \times 4\text{ arcmin}^2$ maps of our pointing target with a continuous Lissajous pattern (Scott et al. 2010), and fitted a bidimensional Gaussian to the resulting map. The calculated offset corrections were not implemented in real time. Instead, they were fed into a time series, and a linearly interpolated offset was applied to the telescope-pointing time series of each COSMOS raster map during the reduction process. A total of 270 pointing observations were obtained for the COSMOS field during the campaign.

AzTEC maps are calibrated using planets as primary calibrators. Each night Uranus or Neptune was imaged in order to derive the flux conversion factor for each detector. In a single observation of a field the typical statistical calibration error is found to be 6–13 per cent (Wilson et al. 2008a). This estimate is supported by the observations of PKS 0537–411, where we report a 6 per cent scatter in 31 single observations (Wilson et al. 2008b).

The COSMOS data presented in this paper are the weighted sum of 203 observations taken over 27 d. If the nightly calibration uncertainty is as high as 13 per cent, in the absence of systematic errors, combining the 27 d of observations leaves us with a statistical calibration uncertainty of 2.5 per cent. Adding this in quadrature with the 5 per cent uncertainty in the brightness temperature of Uranus at 1.1 mm (Griffin & Orton 1993) gives a 5.6 per cent overall calibration uncertainty.

3 DATA REDUCTION

We reduced the AzTEC data in a manner similar to that described in detail by Scott et al. (2008), but with an added set of steps to account for non-linearities in our atmospheric cleaning technique. For each of our 203 observations of the COSMOS field, the raw time-stream data from the instrument, which include both bolometer and pointing data, are despiked and then ‘cleaned’ of atmospheric contamination in a row-by-row manner using our standard principal component analysis technique (see Scott et al. 2008 for a description). An astrometric correction is made to all pointing signals in the time stream based on a linear interpolation of the pointing offsets measured by the bracketing pointing observations of the QSO 1055+018. With this correction in place, the bolometer signals are flux-calibrated and binned into $3 \times 3\text{ arcsec}^2$ pixels. Performing this process for the 203 observations of the field results in 203 nearly independent maps which are then co-added to make a preliminary image of the sky.

As in previous AzTEC analyses, we also produce 100 noise-only realizations of the COSMOS field by jackknifing the time-stream data on a row-by-row basis as described in Scott et al. (2008). These noise maps are used extensively in the characterization of the map properties.

As a deviation from previous AzTEC analyses, we revise the technique presented in Scott et al. (2008), used to estimate the transfer function of the correlated noise removal algorithm on point sources in the data. The previous technique estimated the transfer function by creating simulated data that contain only a point source at the centre of the field and subtracting the eigenmodes identified for removal in the raw time-stream data. The revised technique differs in that the transfer function is estimated by executing the cleaning algorithm on data that combine the raw time-stream data with several simulated point sources distributed throughout the field. In the latter case, the eigenmodes identified for removal are recalculated from

the combination of all sources of signal, noise and simulated point sources. In detail, several Gaussian point sources are added to the time-stream data, all map-making steps save optimal filtering are performed, and the resulting maps are differenced from the original true maps of the sky. The regions near the simulated sources are normalized, stacked and rotationally averaged to produce the point source ‘kernel’. As demonstrated in Downes et al. (2011), this technique provides a better estimation of the effects of the non-linear correlated noise removal on a typical point source in the map. For the COSMOS field, this has the effect of increasing the measured flux and noise values by +15 per cent relative to the values obtained from the prescription in Scott et al. (2008). We use this kernel to optimally filter the maps in an identical manner to that in previous AzTEC analyses.

The final step in the analysis is to use the mean power spectral density of the noise maps and the newly estimated kernel map to construct an optimal filter for point source detection. This final set of Wiener-filtered maps is composed of the filtered signal map, the filtered weight map and the corresponding S/N map. The 100 noise realizations are filtered with the same Wiener filter and will collectively be referred to as ‘noise maps’.

4 1.1-MM MAP AND SOURCE CATALOGUE

4.1 Map

The inner 0.72 deg^2 map of COSMOS acquired by AzTEC at ASTE is shown in Fig. 2. This area corresponds to a minimum coverage of 50 per cent of the maximum coverage attained in the map, and has been shown to provide excellent noise properties for source extraction and overall population analysis (e.g. Scott et al. 2010). The raster scan strategy for COSMOS translates into very uniform noise properties along this section of the map, ranging from 1.23 to 1.27 mJy beam^{-1} , while at the extreme edges of the map (not

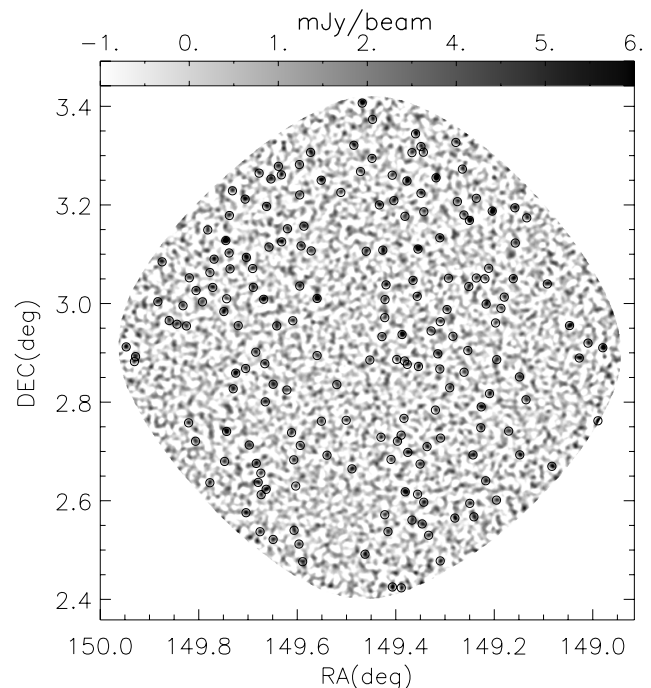


Figure 2. AzTEC 1.1-mm map acquired at ASTE. The circles represent the 189 $S/N \geq 3.5$ source candidates that have been extracted within the 50 per cent coverage area. For reference, the circles have a radius of 30 arcsec.

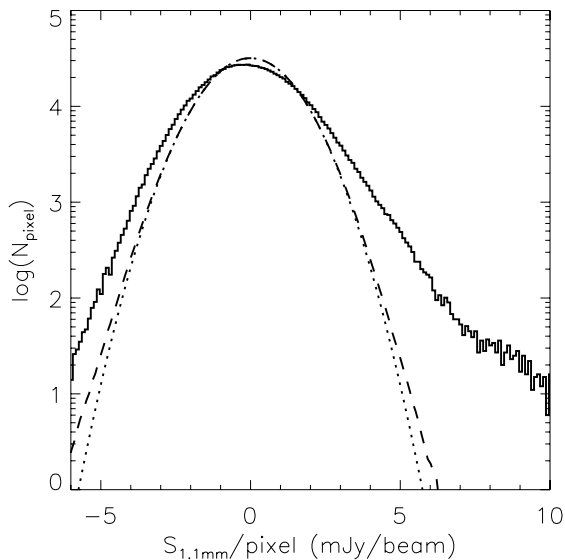


Figure 3. Histogram of flux density values in the AzTEC/ASTE map. The thick solid line represents the values of the signal map over the 50 per cent uniform coverage area. Signal from astronomical sources produces both positive and negative pixels due to the fact that the AzTEC map has a mean of zero (Scott et al. 2008). The dashed line represents the average distribution of flux densities found in 100 jackknifed noise realizations of the field. This distribution is well approximated by a Gaussian function of mean zero and $\sigma \simeq 1.26 \text{ mJy beam}^{-1}$ (dotted line), which we adopt as the average noise level in the uniform coverage area of the map.

represented), the noise increases quickly as one moves away from the centre. The overall noise of the map, characterized by the combined jackknifed noise simulations of the individual raster maps, is well represented by a Gaussian distribution of rms $1.26 \text{ mJy beam}^{-1}$ (see Fig. 3). This value is within the noise range of our previous 0.15 deg^2 COSMOS map (Scott et al. 2008).

4.2 Astrometry

The astrometric accuracy of the AzTEC map is verified by stacking at the positions of 1471 radio sources in the field that are *not* located within 30 arcsec of $7 \pm 3.5\sigma$ or greater peaks in the AzTEC map. The radio source locations are taken from the Very Large Array (VLA) 1.4-GHz deep mosaic of COSMOS (Schinnerer et al. 2010) which has an rms noise level of $15 \mu\text{Jy beam}^{-1}$ in the central $50 \times 50 \text{ arcmin}^2$ region, and positional accuracy better than 1 arcsec . The stacked AzTEC map has a bright, point spread function shaped peak with $S/N = 13$ and an offset from the centre of the stacked image of $0.67 \pm 1.3 \text{ arcsec}$ in RA and $-2.67 \pm 1.3 \text{ arcsec}$ in Dec. Both of these mean offset values are small compared to the 3 arcsec pixel size of the map and so we consider them to be too small to warrant any correction.

4.3 Source catalogue

The source extraction algorithm employed to derive the candidate source catalogue is identical to that used in Scott et al. (2008). We identify point sources in the 1.1-mm S/N map by searching for local maxima within 15 arcsec of pixels with $S/N \geq 3.5$ inside the 50 per cent coverage region. The 189 source candidates are marked with circles in Fig. 2 and listed in Table 1, together with their measured S/N , flux densities, 1σ photometric errors and deboosted flux densities (see Section 6). All sources in the COSMOS catalogue appear to be unresolved.

4.4 False detection rate

The nature of false positives in source identification in AzTEC maps is richly discussed in Perera et al. (2008) and Scott et al. (2010). We follow the same procedure as Scott et al. (2010) and search our 100 noise realizations of the COSMOS field in order to derive a conservative upper limit to the fraction of sources in Table 1 that are actually noise peaks rather than real sources. Fig. 4 shows this upper limit of the fraction of false detections as a function of S/N . The catalogue is robust. At $S/N \geq 3.5$ we derive a mean of 17.4 false detections (9 per cent of the source candidates), and at $S/N \geq 4.0$ we expect only 3 (2 per cent) to be false.

4.5 Completeness

We estimate the completeness of source detections through a set of simulations in which artificial sources of different flux densities are inserted one at a time within the 50 per cent coverage of the observed COSMOS map, and then retrieved with the same source extraction algorithm as that used for building the catalogue. As described in detail by Scott et al. (2008, 2010), this method has the advantage of taking into account the effects of random and confusion noise in the signal map, while it does not alter the properties of the real map significantly. The simulations are based on 1000 test sources per represented flux value. A test source is considered recovered if it is extracted with $S/N \geq 3.5$ at a radius $\leq 17 \text{ arcsec}$ of its input position. This radius is adopted to ensure a ~ 100 per cent recovery of $S/N = 3.5$ sources (see Section 4.6). Fig. 5 summarizes our findings. Sources with flux densities $S_{1.1\text{mm}} \geq 6 \text{ mJy}$ are identified in this survey with ≥ 90 per cent completeness.

4.6 Positional uncertainty

The large beam of ASTE combined with low S/N detections and confusion noise contribute to introducing random offsets in the position in which a source is found in a map. We characterize the positional uncertainty as a function of S/N from the same set of simulations as those used for the completeness calculation, where now we focus on the distance at which the sources get recovered. Fig. 6 shows the uncertainty distribution for sources found in three S/N regimes, and the comparison with the analytical approximation of uncertainties (Ivison et al. 2007), assuming a full width at half-maximum (FWHM) of 34 arcsec for the effective beam of the map: the probability of finding a source at distance $>D$ from its true position is given by $P(>D) = 1 - \exp(-D^2/2\sigma^2)$, where $\sigma = \Delta\alpha = \Delta\delta \approx 0.6 \text{ FWHM} (S/N)^{-1}$. The analytical form shows the same trend as the empirical distribution, and can be used to estimate search radii of possible counterparts of the SMGs presented in this paper.

5 COMPARISON WITH OTHER MAPS

5.1 Overlap with other mm surveys

The AzTEC/ASTE map includes areas of the sky previously imaged by other mm-wavelength surveys, including COSBO (Bertoldi et al. 2007) and AzTEC/JCMT (Scott et al. 2008). Fig. 7 represents the catalogues of these two surveys overlaid on the AzTEC/ASTE map, in order to emphasize common sources and differences among catalogues. Also shown are the unpublished sources detected by Bolocam at the CSO (J. Aguirre, private communication) that are common to the AzTEC catalogue.

Table 1. AzTEC/ASTE source catalogue and ancillary submm to radio photometry. The columns give (1) AzTEC-identification number, (2) source name, (3) S/N of the detection in the AzTEC map, (4) measured 1.1 mm flux density, (5) deboosted flux density and 68 per cent confidence interval, (6) flux density at 890 μ m from the Submillimetre Array (SMA) observations (Younger et al. 2007, 2009), (7) flux density at 1.2 mm from MAMBO (Bertoldi et al. 2007), (8) flux density at 1.4 GHz from VLA (Schinnerer et al. 2010), (9) probability of chance association as per *P*-statistics, (10) angular distance to radio counterpart and (11) notes on individual objects, including names for the source in other (sub)mm catalogues, where AzTEC_J refers to the AzTEC/JCMT catalogue (Scott et al. 2008), AzTEC denotes interferometric SMA detections at 890 μ m (Younger et al. 2007, 2009), MAMBO denotes detections at 1.2 mm by the COSBO survey performed with MAMBO (Bertoldi et al. 2007) and B indicates detection at 1.1 mm by the Bolocam survey carried out at the Caltech Submillimeter Observatory (CSO; J. Aguirre, private communication; for a description of the survey see Aguirre et al. 2006).

AzTEC ID	Source name (MMJ+)	S/N	$S_{1.1\text{ mm}}$ (mJy)	$S_{1.1\text{ mm}}$ (db)	$S_{890\text{ }\mu\text{m}}$ (mJy)	$S_{1.2\text{ mm}}$ (mJy)	$S_{1.4\text{ GHz}}$ (μ Jy)	$P_{1.4\text{ GHz}}$	θ (arcsec)	Notes
AzTEC/C1	100141.70+022711.7	11.5	13.7 \pm 1.2	13.0 ^{+1.1} _{-1.0}						radio associations
AzTEC/C2	095959.20+023450.3	9.9	12.0 \pm 1.2	11.2 ^{+1.1} _{-1.0}	19.7 \pm 1.8					AzTEC_J095959.33+023445.8, AzTEC8, radio associations ^b
AzTEC/C3	100008.00+022609.7	9.3	11.3 \pm 1.2	10.5 ^{+1.0} _{-1.0}	12.4 \pm 1.0		76.0 \pm 14.0	0.003	2.5	AzTEC_J100008.03+022612.1, AzTEC2, B, z = 1.12 ^c
AzTEC/C4	095931.78+023047.2	9.2	11.3 \pm 1.2	10.5 ^{+1.0} _{-1.1}	14.4 \pm 1.9					AzTEC_J095931.83+023040.2, AzTEC4
AzTEC/C5	095942.92+022939.0	8.9	10.8 \pm 1.2	10.0 ^{+1.1} _{-1.1}	15.6 \pm 1.1					AzTEC_J095942.68+022936.0, AzTEC1, radio association ^d , z = 4.65 ^e
AzTEC/C6	100057.20+022008.7	8.7	10.4 \pm 1.2	9.6 ^{+1.1} _{-1.0}		7.5 \pm 1.1	81.0 \pm 15.0	0.007	3.7	MM J100057+022013, B
AzTEC/C7	100015.77+021545.1	8.0	9.7 \pm 1.2	8.9 ^{+1.1} _{-1.1}		6.3 \pm 0.9	73.0 \pm 11.0	0.024	7.0	MM J100016+021549, B
AzTEC/C8	100014.21+015636.1	7.8	9.5 \pm 1.2	8.7 ^{+1.1} _{-1.1}						
AzTEC/C9	100123.24+022002.7	7.5	8.9 \pm 1.2	8.1 ^{+1.0} _{-1.0}			77.0 \pm 16.0	0.012	4.9	B
AzTEC/C10	100013.36+023427.2	7.4	9.0 \pm 1.2	8.1 ^{+1.1} _{-1.1}	4.4 \pm 1.0					AzTEC_J100013.21+023428.2, AzTEC15
AzTEC/C11	100141.28+020357.1	7.3	8.7 \pm 1.2	7.9 ^{+1.1} _{-1.1}						
AzTEC/C12	100136.87+021103.0	7.0	8.4 \pm 1.2	7.5 ^{+1.0} _{-1.1}			144.0 \pm 13.0	0.000	0.9	
AzTEC/C13	095837.91+021408.3	6.8	9.9 \pm 1.5	8.7 ^{+1.3} _{-1.4}			68.0 \pm 13.0	0.002	1.8	AzTEC_J095957.22+022729.3, AzTEC9, B
AzTEC/C14	095957.35+022732.1	6.3	7.7 \pm 1.2	6.7 ^{+1.1} _{-1.1}	9.0 \pm 2.2		131.0 \pm 13.0	0.030	7.9	
AzTEC/C15	100131.67+022509.0	6.2	7.4 \pm 1.2	6.5 ^{+1.1} _{-1.1}			82.0 \pm 14.0	0.010	4.5	
AzTEC/C16	095854.11+021650.5	6.1	7.7 \pm 1.3	6.7 ^{+1.1} _{-1.1}			78.0 \pm 12.0	0.040	9.2	
AzTEC/C17	100055.19+023432.8	5.9	7.1 \pm 1.2	6.2 ^{+1.1} _{-1.1}			98.0 \pm 16.0	0.006	3.5	AzTEC_J100035.37+024352.3, AzTEC12
AzTEC/C18	100035.19+024356.5	5.8	9.4 \pm 1.6	7.9 ^{+1.4} _{-1.6}	13.5 \pm 1.8					
AzTEC/C19	095950.02+015324.0	5.6	7.0 \pm 1.2	5.9 ^{+1.1} _{-1.1}			206.0 \pm 15.0	0.008	4.0	AzTEC_J100008.80+024008.0, AzTEC11, double radio association ^b
AzTEC/C20	100114.46+022702.5	5.6	6.8 \pm 1.2	5.7 ^{+1.2} _{-1.0}			124.0 \pm 14.0	0.013	5.1	
AzTEC/C21	095921.55+022233.5	5.6	6.9 \pm 1.2	5.9 ^{+1.0} _{-1.2}			216.0 \pm 15.0	0.036	8.6	
AzTEC/C22	100009.16+024012.1	5.6	7.5 \pm 1.4	6.4 ^{+1.2} _{-1.3}	4.7 \pm 1.3		100.0 \pm 13.0	0.008	4.0	
AzTEC/C23	100142.65+021833.1	5.6	6.7 \pm 1.2	5.7 ^{+1.0} _{-1.1}			70.0 \pm 12.0	0.050	10.3	
AzTEC/C24	100010.41+022220.9	5.6	6.8 \pm 1.2	5.7 ^{+1.1} _{-1.1}			263.0 \pm 18.0	0.034	8.4	
AzTEC/C25	100122.02+015654.3	5.6	6.7 \pm 1.2	5.7 ^{+1.1} _{-1.1}			133.0 \pm 12.0	0.001	1.2	
AzTEC/C26	100132.27+023214.4	5.5	6.8 \pm 1.2	5.7 ^{+1.2} _{-1.1}			56.0 \pm 11.0	0.020	6.5	AzTEC_J100025.23+022608.0, B
AzTEC/C27	095937.16+020656.5	5.5	6.7 \pm 1.2	5.7 ^{+1.2} _{-1.2}						
AzTEC/C28	095849.35+021253.5	5.4	7.0 \pm 1.3	5.9 ^{+1.2} _{-1.2}						
AzTEC/C29	095918.38+020105.9	5.4	6.7 \pm 1.2	5.6 ^{+1.1} _{-1.1}						
AzTEC/C30	100025.15+022602.2	5.4	6.5 \pm 1.2	5.5 ^{+1.1} _{-1.1}						

Table 1 – continued

AzTEC ID	Source name (MMJ+)	S/N	$S_{1.1\text{ mm}}$ (mJy)	$S_{1.1\text{ mm}}$ (db)	$S_{890\text{ }\mu\text{m}}$ (mJy)	$S_{1.2\text{ mm}}$ (mJy)	$S_{1.4\text{ GHz}}$ (μJy)	$P_{1.4\text{ GHz}}$	θ (arcsec)	Notes
AzTEC/C31	100147.43+022455.9	5.3	6.3 ± 1.2	5.4 ^{+1.1} _{-1.1}						
AzTEC/C32	100012.96+020124.1	5.2	6.4 ± 1.2	5.3 ^{+1.1} _{-1.1}		5.2 ± 2.0	56.0 ± 11.0	0.020	6.5	MM J100012+020125
AzTEC/C33	100026.82+023132.4	5.2	6.3 ± 1.2	5.3 ^{+1.1} _{-1.1}			67.0 ± 12.0	0.043	9.5	AzTEC_J100026.68+023128.1
AzTEC/C34	100007.77+021151.6	5.2	6.3 ± 1.2	5.3 ^{+1.1} _{-1.2}		5.7 ± 0.9				MM J100007+021149
AzTEC/C35	100008.37+022024.3	5.1	6.2 ± 1.2	5.2 ^{+1.1} _{-1.1}			62.0 ± 12.0	0.041	9.3	
AzTEC/C36	095840.29+020514.7	5.1	8.6 ± 1.7	6.8 ^{+1.5} _{-1.6}			168.0 ± 15.0	0.000	0.2	
AzTEC/C37	100121.82+023121.3	5.1	6.1 ± 1.2	5.1 ^{+1.1} _{-1.1}			52.0 ± 8.0	0.031	8.0	
AzTEC/C38	100023.58+022148.2	5.1	6.2 ± 1.2	5.1 ^{+1.2} _{-1.1}			43.0 ± 11.0	0.025	7.2	
AzTEC/C39	100126.84+020003.3	5.1	6.1 ± 1.2	5.1 ^{+1.1} _{-1.1}			64.0 ± 11.0	0.063	11.6	
AzTEC/C40	095934.76+021927.6	5.0	6.1 ± 1.2	5.1 ^{+1.1} _{-1.2}						
AzTEC/C41	100148.08+022129.3	5.0	6.0 ± 1.2	4.9 ^{+1.1} _{-1.1}						
AzTEC/C42	100019.75+023203.4	4.9	5.9 ± 1.2	4.8 ^{+1.1} _{-1.1}	9.3 ± 1.1		126.0 ± 15.0	0.000	0.9	AzTEC_J100019.73+023206.0, AzTEC5, z = 3.97 ^c
AzTEC/C43	100003.58+020206.1	4.9	6.0 ± 1.2	4.8 ^{+1.2} _{-1.1}			85.0 ± 15.0	0.028	7.7	
AzTEC/C44	100033.80+014900.2	4.9	6.2 ± 1.3	5.0 ^{+1.2} _{-1.2}			84.0 ± 11.0	0.032	8.2	
AzTEC/C45	100006.54+023257.1	4.9	6.0 ± 1.2	4.8 ^{+1.1} _{-1.1}						
AzTEC/C46	100114.61+023511.9	4.9	6.0 ± 1.2	4.8 ^{+1.2} _{-1.1}			122.0 ± 12.0	0.021	6.7	
AzTEC/C47	095941.18+020105.6	4.9	5.9 ± 1.2	4.8 ^{+1.1} _{-1.1}			222.0 ± 11.0	0.038	9.0	
AzTEC/C48	100039.24+023847.9	4.9	6.1 ± 1.2	4.9 ^{+1.2} _{-1.2}			63.0 ± 13.0	0.003	2.5	AzTEC_J100038.72+023843.8
AzTEC/C49	100131.83+015403.3	4.9	6.5 ± 1.3	5.3 ^{+1.2} _{-1.3}			57.0 ± 10.0	0.001	1.1	
AzTEC/C50	095933.13+020833.2	4.8	5.9 ± 1.2	4.8 ^{+1.2} _{-1.2}						
AzTEC/C51	100040.19+015923.7	4.8	5.8 ± 1.2	4.7 ^{+1.1} _{-1.1}			119.0 ± 15.0	0.026	7.3	
AzTEC/C52	100156.23+022106.3	4.8	5.7 ± 1.2	4.7 ^{+1.1} _{-1.1}						
AzTEC/C53	100122.65+021211.8	4.8	5.7 ± 1.2	4.6 ^{+1.1} _{-1.1}						
AzTEC/C54	100125.89+015744.6	4.8	5.7 ± 1.2	4.6 ^{+1.1} _{-1.1}			65.0 ± 11.0	0.074	12.5	
AzTEC/C55	100005.19+015520.0	4.8	5.8 ± 1.2	4.7 ^{+1.1} _{-1.2}						
AzTEC/C56	095904.93+022154.6	4.7	5.8 ± 1.2	4.7 ^{+1.1} _{-1.1}						
AzTEC/C57	095958.34+021324.4	4.7	5.7 ± 1.2	4.6 ^{+1.2} _{-1.2}			82.0 ± 12.0	0.049	10.2	
AzTEC/C58	100020.47+014500.6	4.7	7.3 ± 1.6	5.6 ^{+1.4} _{-1.5}			59.0 ± 13.0	0.019	6.3	
AzTEC/C59	100030.40+023712.2	4.7	6.9 ± 1.2	4.6 ^{+1.2} _{-1.2}			161.0 ± 15.0	0.018	6.1	
AzTEC/C60	100128.29+022129.7	4.6	5.5 ± 1.2	4.4 ^{+1.1} _{-1.1}						
AzTEC/C61	100119.68+023442.0	4.6	5.7 ± 1.2	4.6 ^{+1.2} _{-1.1}			10350 ± 1000	0.018	9.1	extended
AzTEC/C62	100100.37+023756.3	4.6	5.9 ± 1.3	4.7 ^{+1.2} _{-1.2}						
AzTEC/C63	095920.75+023111.3	4.6	6.1 ± 1.3	4.8 ^{+1.3} _{-1.3}						
AzTEC/C64	100139.64+022345.2	4.6	5.5 ± 1.2	4.4 ^{+1.1} _{-1.1}						

Table 1 – continued

AzTEC ID	Source name (MMJ+)	S/N	$S_{1.1\text{mm}}$ (mJy)	$S_{1.1\text{mm}}$ (db)	$S_{890\mu\text{m}}$ (mJy)	$S_{1.2\text{mm}}$ (mJy)	$S_{1.4\text{GHz}}$ (μJy)	$P_{1.4\text{GHz}}$	θ (arcsec)	Notes
AzTEC/C65	095943.22+022136.1	4.6	5.6 ± 1.2	$4.4_{-1.2}^{+1.2}$			153.0 ± 12.0	0.046	9.8	
AzTEC/C66	100105.00+022632.7	4.6	5.5 ± 1.2	$4.3_{-1.1}^{+1.1}$			86.0 ± 11.0	0.015	5.5	
AzTEC/C67	100118.61+020941.7	4.6	5.5 ± 1.2	$4.3_{-1.1}^{+1.1}$						
AzTEC/C68	100122.43+020733.5	4.6	5.5 ± 1.2	$4.3_{-1.1}^{+1.1}$						
AzTEC/C69	100138.07+020908.9	4.6	5.5 ± 1.2	$4.3_{-1.1}^{+1.1}$			547.0 ± 13.0	0.022	6.8	
AzTEC/C70	100026.04+020314.9	4.5	5.5 ± 1.2	$4.3_{-1.1}^{+1.1}$			49.0 ± 13.0	0.037	8.8	
AzTEC/C71	095953.83+021847.9	4.5	5.5 ± 1.2	$4.3_{-1.1}^{+1.1}$		5.7 ± 1.3	79.0 ± 11.0	0.017	6.0	MM J095953+021851, B
AzTEC/C72	100159.82+020459.8	4.5	5.6 ± 1.2	$4.4_{-1.2}^{+1.2}$						
AzTEC/C73	100103.62+022856.8	4.5	5.4 ± 1.2	$4.2_{-1.1}^{+1.1}$						
AzTEC/C74	100105.64+022139.6	4.5	5.4 ± 1.2	$4.2_{-1.1}^{+1.1}$			91.0 ± 12.0	0.025	7.3	
AzTEC/C75	100052.35+020103.1	4.4	5.3 ± 1.2	$4.2_{-1.2}^{+1.2}$						
AzTEC/C76	100013.21+021207.0	4.4	5.4 ± 1.2	$4.2_{-1.1}^{+1.1}$						
AzTEC/C77	095935.00+015756.7	4.4	5.4 ± 1.2	$4.2_{-1.1}^{+1.2}$			69.0 ± 11.0	0.014	5.4	
AzTEC/C78	095902.73+015942.0	4.4	6.5 ± 1.5	$4.8_{-1.3}^{+1.3}$						
AzTEC/C79	095943.70+021348.3	4.4	5.4 ± 1.2	$4.2_{-1.2}^{+1.2}$						
AzTEC/C80	100033.24+022553.6	4.4	5.3 ± 1.2	$4.1_{-1.1}^{+1.1}$						
AzTEC/C81	100005.97+015241.4	4.4	5.4 ± 1.2	$4.1_{-1.1}^{+1.2}$						
AzTEC/C82	100116.85+021648.4	4.4	5.2 ± 1.2	$4.1_{-1.2}^{+1.2}$						
AzTEC/C83	100230.25+021414.6	4.3	6.8 ± 1.6	$4.9_{-1.5}^{+1.5}$						
AzTEC/C84	095942.76+015511.7	4.3	5.3 ± 1.2	$4.1_{-1.2}^{+1.2}$						
AzTEC/C85	100140.09+022541.3	4.3	5.2 ± 1.2	$4.0_{-1.1}^{+1.1}$			549.0 ± 12.0	0.039	9.0	
AzTEC/C86	100109.03+021726.0	4.3	5.2 ± 1.2	$4.0_{-1.1}^{+1.1}$			4210 ± 400	0.016	5.7	extended
AzTEC/C87	100205.50+021700.1	4.3	5.2 ± 1.2	$4.0_{-1.2}^{+1.2}$						
AzTEC/C88	095937.37+020423.9	4.3	5.3 ± 1.2	$4.0_{-1.1}^{+1.1}$						
AzTEC/C89	100127.08+021336.1	4.3	5.1 ± 1.2	$4.0_{-1.1}^{+1.1}$						
AzTEC/C90	100135.64+021650.2	4.3	5.1 ± 1.2	$4.0_{-1.2}^{+1.2}$			81.0 ± 12.0	0.038	8.9	
AzTEC/C91	100128.61+022347.4	4.2	5.1 ± 1.2	$3.8_{-1.2}^{+1.2}$						
AzTEC/C92	100139.94+023015.0	4.2	5.2 ± 1.2	$4.0_{-1.1}^{+1.1}$			60.0 ± 11.0	0.004	2.8	
AzTEC/C93	100132.02+021137.0	4.2	5.1 ± 1.5	$3.8_{-1.1}^{+1.1}$						
AzTEC/C94	095957.13+021719.0	4.2	5.1 ± 1.2	$3.9_{-1.1}^{+1.1}$						
AzTEC/C95	100018.36+021242.9	4.2	5.1 ± 1.2	$3.8_{-1.1}^{+1.1}$						
AzTEC/C96	100108.38+015154.6	4.2	5.2 ± 1.2	$3.9_{-1.2}^{+1.2}$						
AzTEC/C97	100214.84+021944.9	4.2	5.5 ± 1.3	$4.1_{-1.3}^{+1.3}$			55.0 ± 16.0	0.013	5.1	
AzTEC/C98	100042.99+020518.4	4.2	5.0 ± 1.2	$3.8_{-1.2}^{+1.2}$			78.0 ± 14.0	0.005	3.1	

Table 1 – *continued*

AzTEC ID	Source name (MMJ+)	S/N	$S_{1.1\text{ mm}}$ (m)	$S_{1.1\text{ mm}}$ (mJy)	$S_{1.1\text{ mm}}$ (db)	$S_{890\text{ }\mu\text{m}}$ (mJy)	$S_{1.2\text{ mm}}$ (mJy)	$S_{1.4\text{ GHz}}$ (μJy)	$P_{1.4\text{ GHz}}$	θ (arcsec)	Notes
AzTEC/C99	100006.98+015958.9	4.2	5.1 ± 1.2	3.8 ^{+1.1} _{-1.2}							
AzTEC/C100	095918.52+021035.8	4.2	5.1 ± 1.2	3.8 ^{+1.2} _{-1.1}							
AzTEC/C101	095945.58+023018.5	4.2	5.1 ± 1.2	3.8 ^{+1.1} _{-1.2}							
AzTEC/C102	095948.77+023156.5	4.1	5.1 ± 1.2	3.8 ^{+1.1} _{-1.2}							
AzTEC/C103	100124.43+015615.1	4.1	5.0 ± 1.2	3.8 ^{+1.1} _{-1.2}				51.0 ± 15.0	0.036	8.7	
AzTEC/C104	095940.74+015333.1	4.1	5.3 ± 1.3	4.0 ^{+1.2} _{-1.3}							
AzTEC/C105	095845.11+021442.1	4.1	5.5 ± 1.3	4.1 ^{+1.2} _{-1.3}							
AzTEC/C106	100006.54+023838.6	4.1	5.3 ± 1.3	4.0 ^{+1.2} _{-1.3}		8.6 ± 1.3					AzTEC_J100006.40+023839.8, AzTEC6
AzTEC/C107	095939.56+022238.3	4.1	5.0 ± 1.2	3.8 ^{+1.1} _{-1.2}							
AzTEC/C108	100116.05+023614.3	4.1	5.3 ± 1.3	4.0 ^{+1.2} _{-1.3}							
AzTEC/C109	100111.63+022838.3	4.1	5.0 ± 1.2	3.7 ^{+1.1} _{-1.1}				59.0 ± 11.0	0.004	2.7	
AzTEC/C110	100108.56+020029.7	4.1	5.0 ± 1.2	3.7 ^{+1.1} _{-1.1}				67.0 ± 12.0	0.019	6.3	
AzTEC/C111	095929.62+021241.6	4.1	5.0 ± 1.2	3.7 ^{+1.2} _{-1.2}				122.0 ± 12.0	0.014	5.3	
AzTEC/C112	100010.94+015309.3	4.1	5.0 ± 1.2	3.7 ^{+1.1} _{-1.2}				173.0 ± 16.0	0.036	8.7	
AzTEC/C113	095914.96+022957.7	4.1	5.5 ± 1.3	4.0 ^{+1.3} _{-1.3}							
AzTEC/C114	100024.06+022000.6	4.1	4.9 ± 1.2	3.7 ^{+1.1} _{-1.2}							
AzTEC/C115	100014.84+020532.5	4.1	4.9 ± 1.2	3.7 ^{+1.1} _{-1.2}							
AzTEC/C116	100109.63+020348.3	4.0	4.9 ± 1.2	3.7 ^{+1.1} _{-1.2}			4.2 ± 1.4	59.0 ± 11.0	0.008	4.0	MM J100109+020346
AzTEC/C117	095925.93+022018.3	4.0	5.0 ± 1.2	3.7 ^{+1.1} _{-1.2}							
AzTEC/C118	095959.49+020633.1	4.0	4.9 ± 1.2	3.7 ^{+1.1} _{-1.2}				104.0 ± 13.0	0.023	6.9	MM J100000+020634, B
AzTEC/C119	095915.34+020748.3	4.0	5.0 ± 1.2	3.7 ^{+1.1} _{-1.2}							
AzTEC/C120	100105.38+020214.6	4.0	4.9 ± 1.2	3.6 ^{+1.1} _{-1.1}							
AzTEC/C121	095952.53+020915.9	4.0	4.9 ± 1.2	3.7 ^{+1.1} _{-1.2}							
AzTEC/C122	100200.88+021648.0	4.0	4.8 ± 1.2	3.6 ^{+1.1} _{-1.2}							
AzTEC/C123	100022.62+015145.4	4.0	4.9 ± 1.2	3.7 ^{+1.1} _{-1.2}							
AzTEC/C124	095946.32+023554.0	4.0	5.1 ± 1.3	3.7 ^{+1.2} _{-1.2}				27.0 ± 13.0	0.038	8.9	AzTEC_J095946.66+023541.9
AzTEC/C125	095920.54+022653.8	4.0	4.9 ± 1.2	3.6 ^{+1.2} _{-1.2}				18059 ± 1800	0.033	8.3	extended
AzTEC/C126	100159.48+022239.4	4.0	4.8 ± 1.2	3.5 ^{+1.2} _{-1.2}				134.0 ± 13.0	0.048	10.1	
AzTEC/C127	100125.46+023524.3	4.0	5.4 ± 1.3	3.8 ^{+1.3} _{-1.3}				131.0 ± 12.0	0.007	3.9	
AzTEC/C128	100002.80+015118.3	4.0	4.9 ± 1.2	3.6 ^{+1.2} _{-1.2}							
AzTEC/C129	100130.23+020217.6	4.0	4.7 ± 1.2	3.5 ^{+1.1} _{-1.1}							B
AzTEC/C130	095956.99+020308.4	3.9	4.8 ± 1.2	3.5 ^{+1.1} _{-1.2}				124.0 ± 10.0	0.018	6.1	
AzTEC/C131	100010.93+023754.3	3.9	4.9 ± 1.2	3.5 ^{+1.2} _{-1.2}							
AzTEC/C132	100005.35+023757.4	3.9	4.9 ± 1.3	3.5 ^{+1.2} _{-1.2}							
AzTEC/C133	100120.64+022624.4	3.9	4.7 ± 1.2	3.4 ^{+1.1} _{-1.2}				79.0 ± 12.0	0.006	3.4	

Table 1 – continued

AzTEC ID	Source name (MMJ+)	S/N	$S_{1.1\text{mm}}$ (mJy)	$S_{1.1\text{mm}}$ (db)	$S_{890\mu\text{m}}$ (mJy)	$S_{1.2\text{mm}}$ (mJy)	$S_{1.4\text{GHz}}$ (μJy)	$P_{1.4\text{GHz}}$	θ (arcsec)	Notes
AzTEC/C134	100106.01+015014.2	3.9	5.0 ± 1.3	3.6 ^{+1.2} _{-1.3}						
AzTEC/C135	100024.18+015348.4	3.9	4.7 ± 1.2	3.4 ^{+1.2} _{-1.2}						
AzTEC/C136	095933.52+022348.9	3.9	4.7 ± 1.2	3.4 ^{+1.2} _{-1.2}			76.0 ± 14.0	0.001	1.6	
AzTEC/C137	095953.11+022236.1	3.9	4.7 ± 1.2	3.4 ^{+1.2} _{-1.2}						
AzTEC/C138	100020.54+023509.3	3.9	4.7 ± 1.2	3.4 ^{+1.1} _{-1.2}	8.7 ± 1.5					AzTEC_J100020.71+023518.2, AzTEC3, z = 5.3 ^c
AzTEC/C139	100202.55+021915.3	3.9	4.7 ± 1.2	3.4 ^{+1.1} _{-1.2}						
AzTEC/C140	100124.98+015144.4	3.9	5.4 ± 1.4	3.7 ^{+1.3} _{-1.4}			49.0 ± 11.0	0.004	2.9	
AzTEC/C141	100209.29+021727.3	3.9	4.7 ± 1.2	3.4 ^{+1.1} _{-1.2}						
AzTEC/C142	100018.01+020245.5	3.8	4.7 ± 1.2	3.3 ^{+1.2} _{-1.2}						
AzTEC/C143	100149.44+015742.3	3.8	5.4 ± 1.4	3.7 ^{+1.3} _{-1.4}						
AzTEC/C144	100142.27+020017.7	3.8	4.6 ± 1.2	3.3 ^{+1.1} _{-1.2}			247.0 ± 12.0	0.012	5.1	
AzTEC/C145	100031.47+021239.0	3.8	4.6 ± 1.2	3.3 ^{+1.1} _{-1.2}		5.3 ± 0.9	189.0 ± 10.0	0.023	6.9	MM J100031+021241
AzTEC/C146	095957.15+014811.0	3.8	5.6 ± 1.5	3.7 ^{+1.5} _{-1.4}			77.0 ± 13.0	0.025	7.2	
AzTEC/C147	100107.60+015718.3	3.8	4.6 ± 1.2	3.2 ^{+1.2} _{-1.2}						
AzTEC/C148	100025.56+021530.1	3.8	4.6 ± 1.2	3.3 ^{+1.2} _{-1.2}						
AzTEC/C149	100150.50+022829.7	3.8	4.9 ± 1.3	3.4 ^{+1.2} _{-1.3}		4.9 ± 0.9				MM J100026+021529
AzTEC/C150	100005.15+023042.3	3.8	4.6 ± 1.2	3.3 ^{+1.2} _{-1.2}			95.0 ± 11.0	0.026	7.3	
AzTEC/C151	095950.96+021532.3	3.8	4.6 ± 1.2	3.2 ^{+1.2} _{-1.2}			96.0 ± 15.0	0.016	5.8	AzTEC_J100004.54+023040.1
AzTEC/C152	100030.16+024157.3	3.8	5.3 ± 1.4	3.6 ^{+1.4} _{-1.4}						
AzTEC/C153	100212.74+022436.2	3.8	5.7 ± 1.5	3.7 ^{+1.5} _{-1.5}			193.0 ± 15.0	0.032	8.2	
AzTEC/C154	100036.01+023536.0	3.8	4.6 ± 1.2	3.2 ^{+1.2} _{-1.2}			72.0 ± 14.0	0.046	9.8	
AzTEC/C155	100055.08+020511.8	3.8	4.5 ± 1.2	3.2 ^{+1.1} _{-1.2}						
AzTEC/C156	100225.69+021303.8	3.8	5.5 ± 1.5	3.7 ^{+1.4} _{-1.5}						
AzTEC/C157	100104.22+014805.5	3.8	5.3 ± 1.4	3.6 ^{+1.4} _{-1.4}					11.1	
AzTEC/C158	100014.58+021232.3	3.7	4.5 ± 1.2	3.2 ^{+1.1} _{-1.2}			114.0 ± 12.0	0.059		
AzTEC/C159	095929.75+015535.4	3.7	4.8 ± 1.3	3.3 ^{+1.3} _{-1.3}						
AzTEC/C160	100024.20+021748.7	3.7	4.5 ± 1.2	3.1 ^{+1.2} _{-1.2}						
AzTEC/C161	095939.54+023220.5	3.7	4.5 ± 1.2	3.1 ^{+1.2} _{-1.2}		5.2 ± 0.9	83.0 ± 12.0	0.005	3.3	MM J100024+021748
AzTEC/C162	100001.59+021611.2	3.7	4.5 ± 1.2	3.1 ^{+1.2} _{-1.2}		5.2 ± 0.9	83.0 ± 12.0	0.005	3.3	
AzTEC/C163	100124.60+015851.8	3.7	4.4 ± 1.2	3.1 ^{+1.1} _{-1.2}						
AzTEC/C164	095935.35+022232.8	3.7	4.5 ± 1.2	3.1 ^{+1.2} _{-1.2}						
AzTEC/C165	095949.52+023908.9	3.7	5.4 ± 1.5	3.5 ^{+1.4} _{-1.5}						
AzTEC/C166	100105.81+023627.3	3.7	4.5 ± 1.2	3.1 ^{+1.2} _{-1.2}						
AzTEC/C167	095923.81+020359.5	3.7	4.5 ± 1.2	3.1 ^{+1.2} _{-1.3}						

Table 1 – *continued*

AzTEC ID	Source name (MMJ+)	S/N	$S_{1.1\text{ mm}}$ (mJy)	$S_{1.1\text{ mm}}$ (db)	$S_{890\ \mu\text{m}}$ (mJy)	$S_{1.2\text{ mm}}$ (mJy)	$S_{1.4\text{ GHz}}$ (μJy)	$P_{1.4\text{ GHz}}$	θ (arcsec)	Notes
AzTEC/C168	100057.18+021311.7	3.7	4.4 ± 1.2	3.0 ^{+1.2} _{-1.2}						MM J100057+021305
AzTEC/C169	100014.35+023009.0	3.7	4.4 ± 1.2	3.1 ^{+1.1} _{-1.2}						
AzTEC/C170	100045.62+023303.6	3.7	4.4 ± 1.2	3.0 ^{+1.2} _{-1.2}						
AzTEC/C171	100047.57+020939.4	3.6	4.4 ± 1.2	3.0 ^{+1.2} _{-1.2}			362.0 ± 13.0	0.002	1.9	
AzTEC/C172	100021.15+020032.3	3.6	4.4 ± 1.2	3.0 ^{+1.2} _{-1.2}						
AzTEC/C173	100118.61+015047.9	3.6	5.0 ± 1.4	3.3 ^{+1.4} _{-1.4}						
AzTEC/C174	100008.19+015618.1	3.6	4.4 ± 1.2	3.0 ^{+1.2} _{-1.2}			50.0 ± 9.0	0.017	5.9	
AzTEC/C175	100156.44+020245.4	3.6	4.6 ± 1.3	3.1 ^{+1.2} _{-1.3}						
AzTEC/C176	095957.35+021133.2	3.6	4.4 ± 1.2	3.0 ^{+1.2} _{-1.2}		6.0 ± 1.1	60.0 ± 11.0	0.013	5.2	MM J095956+021139
AzTEC/C177	100138.47+023315.4	3.6	5.1 ± 1.4	3.2 ^{+1.4} _{-1.4}						
AzTEC/C178	100141.28+022006.6	3.6	4.3 ± 1.2	2.9 ^{+1.2} _{-1.2}			83.0 ± 13.0	0.010	4.5	
AzTEC/C179	100149.44+022318.4	3.6	4.3 ± 1.2	2.9 ^{+1.2} _{-1.2}						
AzTEC/C180	095927.55+021856.5	3.6	4.4 ± 1.2	3.0 ^{+1.1} _{-1.3}						
AzTEC/C181	095930.18+021709.7	3.6	4.4 ± 1.2	2.9 ^{+1.2} _{-1.2}			54.0 ± 10.0	0.047	10.0	
AzTEC/C182	100016.21+020329.7	3.6	4.3 ± 1.2	2.9 ^{+1.2} _{-1.2}						
AzTEC/C183	100226.23+021227.1	3.6	5.3 ± 1.5	3.3 ^{+1.4} _{-1.6}						
AzTEC/C184	100016.14+014454.3	3.6	5.8 ± 1.6	3.5 ^{+1.6} _{-1.8}						
AzTEC/C185	100111.89+020859.8	3.6	4.3 ± 1.2	2.9 ^{+1.1} _{-1.3}			71.0 ± 15.0	0.000	0.8	
AzTEC/C186	100105.68+023245.3	3.5	4.3 ± 1.2	2.9 ^{+1.1} _{-1.2}			83.0 ± 16.0	0.003	2.6	
AzTEC/C187	100153.08+021944.0	3.5	4.2 ± 1.2	2.9 ^{+1.1} _{-1.3}			93.0 ± 14.0	0.054	10.7	B
AzTEC/C188	095945.52+021109.7	3.5	4.3 ± 1.2	2.9 ^{+1.2} _{-1.3}						
AzTEC/C189	100100.06+022556.3	3.5	4.2 ± 1.2	2.8 ^{+1.2} _{-1.2}			82.0 ± 15.0	0.025	7.2	

Note. Also included in the 'Notes' column are claims for additional radio associations and spectroscopic redshifts, where references are "Smolčić et al. (2011), ^dYounger et al. (2009), ^eCapak et al. (in preparation), ^dYounger et al. (2007) and ^eCapak et al. (2011), Riechers et al. (2010).

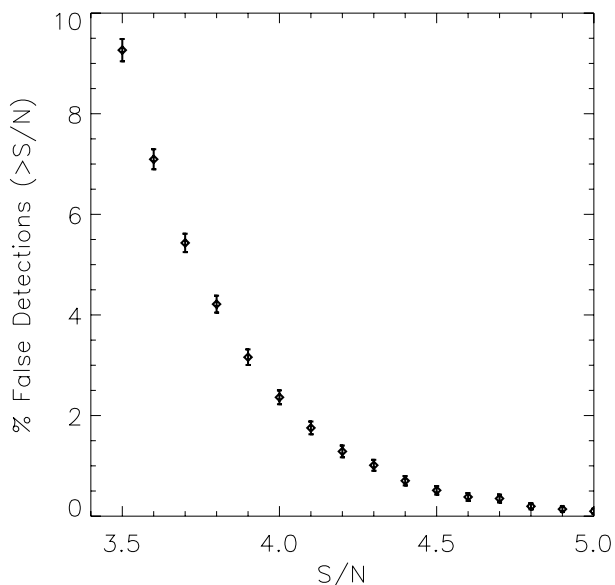


Figure 4. Expected fraction of false detections in the AzTEC catalogue as a function of limiting S/N estimated through counting peaks in 100 noise-only realizations of the field.

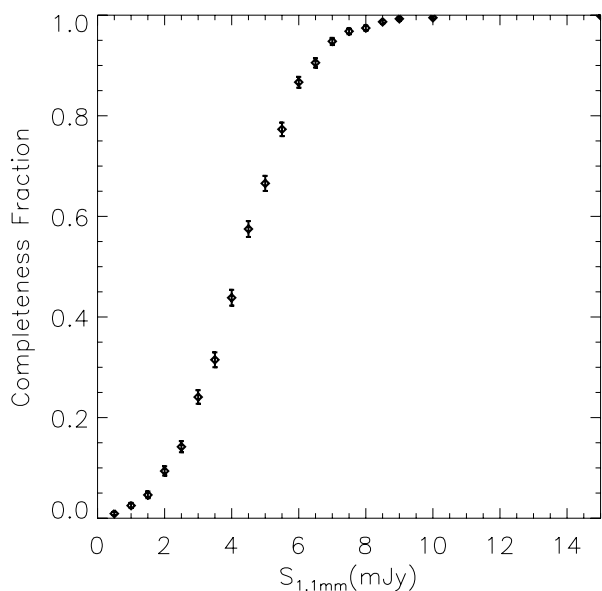


Figure 5. Survey completeness estimates for the COSMOS catalogue as a function of flux density. The points and 68 per cent binomial error bars show the completeness estimated by inserting sources of known flux density one at a time into the observed signal map and then finding them with the same source extraction algorithm as that used to create the candidate source catalogue. In order for a source to be considered recovered, it must be detected with $S/N \geq 3.5$ at a distance $r \leq 17$ arcsec from the input location.

The AzTEC/ASTE and AzTEC/JCMT surveys have similar noise properties with rms ~ 1.25 mJy beam $^{-1}$. The 10-m ASTE image, however, has a resolution of 34 arcsec, while the JCMT image has an effective resolution of 18 arcsec, after Wiener filtering. Due to the considerable level of incompleteness at low S/N in both catalogues, not all sources are expected to be found in both. Out of the 50 candidate sources extracted from the AzTEC/JCMT survey at $S/N \geq 3.5$, 48 fall within an overlapping region with the AzTEC/ASTE survey. In order to find which entries in the catalogues match each other,

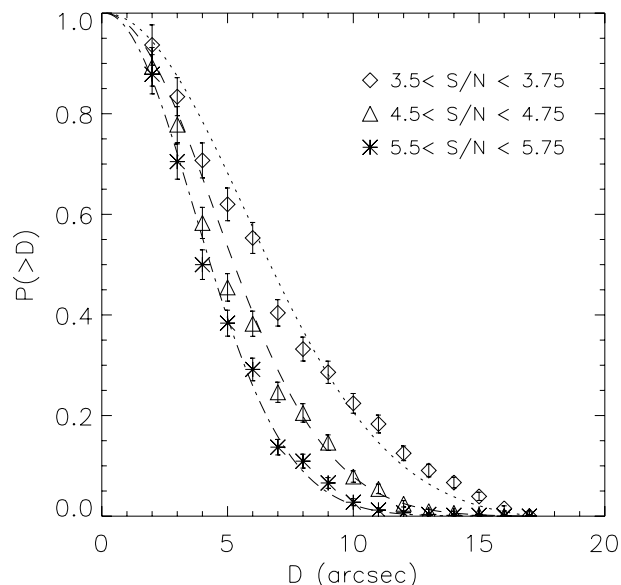


Figure 6. Positional uncertainty distributions for AzTEC/ASTE source candidates. The data points and 68 per cent confidence intervals show the probability $P(>D)$ that AzTEC sources of different S/N will be found outside a radial distance D , as determined from simulations. The curves show the expected probabilities from the simple approximation that takes into account the beam size and the S/N of the detection (Ivison et al. 2007).

we adopt the positional uncertainty relation that depends on the effective beam size and S/N of the detections (Section 4.6). This relationship has been shown to work well for both the AzTEC/JCMT (Scott et al. 2008) and ASTE data (Fig. 6). Since a real source will suffer from positional uncertainties in both catalogues, we will use for each ASTE source a search radius at the 95 per cent confidence level of containing the location of the real source, and will add in quadrature the 95 per cent confidence positional uncertainty radius of a potentially matching JCMT source. If the distance between the JCMT and ASTE catalogue positions is smaller than the resulting search radius, both catalogue entries will be considered to correspond to the same source. Search radii derived in this manner range from 6.4 to 13.6 arcsec. A candidate source that is found in two independent data sets also increases its individual reliability over the average false detection rate corresponding to its nominal S/N. Out of the 48 AzTEC/JCMT source candidates that fall within the ASTE surveyed area, 16 are common to the ASTE catalogue, and are listed in Table 1.

The coincidence between the bright AzTEC/ASTE and AzTEC/JCMT sources is remarkable. From the list of the 15 brightest AzTEC/JCMT sources that were followed up and confirmed with SMA (Younger et al. 2007, 2009), only AzTEC 13 and 14 are not found in the AzTEC/ASTE catalogue. Both sources have deboosted flux densities $S_{1.1\text{mm}} \approx 4.47 \pm 1.3$ mJy (Scott et al. 2008). At these flux densities, the completeness estimated for the AzTEC/ASTE map indicates a ~ 57 per cent chance of recovery. The other two sources in this flux range, AzTEC/JCMT 11 and 12, are indeed detected. The level of recovery at lower flux densities is lower, as expected by the completeness function.

Fig. 8 represents the deboosted fluxes of the AzTEC/ASTE map versus the deboosted fluxes of the AzTEC/JCMT revised catalogue (Downes et al. 2011). The filtering and deboosting methods employed were exactly the same for both data sets. The mean ratio between fluxes is 1.08, with an rms of 0.44. Folded into these

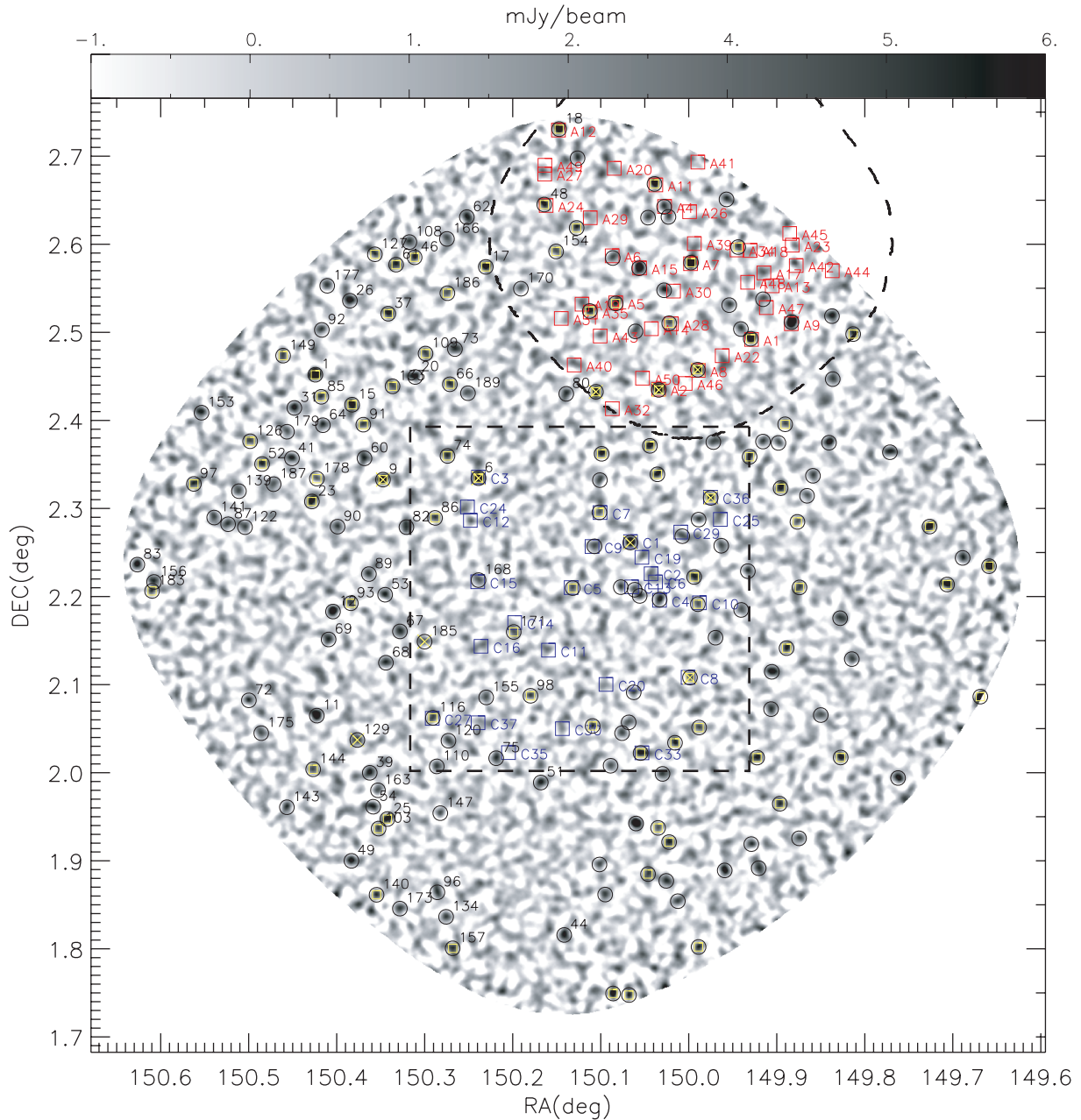


Figure 7. AzTEC map and comparison with other mm catalogues. Circles and numbers denote AzTEC sources from this work. Blue and red squares denote COSBO (Bertoldi et al. 2007) and AzTEC/JCMT (Scott et al. 2008) sources, with accompanying labels C# and A# that refer to their catalogue numbers, respectively. The boundaries of the surveys are marked with dashed lines. The AzTEC sources from this work also detected by the Bolocam survey are marked with crosses (Aguirre et al., private communication). AzTEC sources from this work robustly associated with 1.4 GHz sources in this or other works are marked with inner yellow squares.

discrepancies are the increased noise in the new filtering technique, blending of fainter sources within the larger ASTE beam and the impact of these effects on the deboosting process.

At 1.2 mm the COSBO survey derived a catalogue of 27 candidate sources detected at $S_{1.2\text{mm}} \gtrsim 2.2$ mJy, out of which 12 have AzTEC/ASTE 1.1 mm counterparts, following a positional uncertainty analysis similar to that performed above. The FWHM for the MAMBO map has been adopted to be 11 arcsec, and the resulting search radii at 95 per cent confidence level range between 6.2 and 14.0 arcsec. Common sources are listed in Table 1. The mean deboosted flux density ratio for these common sources is

$S_{1.1\text{mm}}/S_{1.2\text{mm}} = 0.93 \pm 0.43$. Among the 15 brightest COSBO sources, with $S_{1.2\text{mm}} \gtrsim 4.4$ mJy, COSBO ID numbers 2, 6, 11, 12 and 14 are not formally detected in our AzTEC/ASTE catalogue, although they show $2.4 \lesssim S/N \lesssim 3.4$ peaks in the AzTEC S/N map. For instance, COSBO source 2, $S_{1.2\text{mm}} \gtrsim 5.9$ mJy (Bertoldi et al. 2007), has a probability of detection in the AzTEC/ASTE map of ~ 90 per cent (assuming a 0.93 mean flux ratio), and, indeed, has a $S/N \approx 3.0$ in the AzTEC/ASTE map at the COSBO position.

From the catalogue of 19 candidate sources extracted by the Bolocam team, 10 are also detected by the deeper AzTEC/ASTE survey, and are identified in Table 1. The adopted effective FWHM

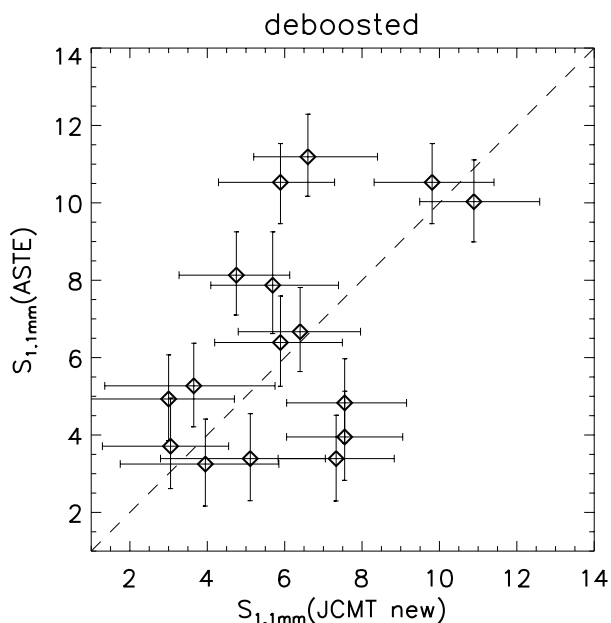


Figure 8. Deboosted ASTE versus deboosted JCMT fluxes corresponding to the common sources between this paper and the revised catalogue published in Downes et al. (2011). Error bars represent 68 per cent confidence intervals in deboosted fluxes.

for the Bolocam map in the positional uncertainty calculation to match AzTEC/ASTE sources is 31 arcsec (Laurent et al. 2005), and the resulting search radii range between 10.9 and 18.7 arcsec.

5.2 Overlap with the deep COSMOS radio survey

The VLA 1.4-GHz deep mosaic of COSMOS (Schinnerer et al. 2010) also provides an excellent catalogue to look for counterparts of the SMGs presented in this paper. The tight correlation between radio continuum emission, which is dominated by synchrotron radiation from supernova remnants, and FIR emission dominated by thermal radiation from warm dust heated by young stars in galaxies (Helou, Soifer & Rowan-Robinson 1985; Condon 1992; Yun, Reddy & Condon 2001) translates into a large percentage of cross-identifications among catalogues derived in both frequencies (e.g. Ivison et al. 2002, 2007).

The matching process was carried out within 17 arcsec radii circles of the AzTEC positions, looking for possible associations. To quantify the significance of the possible associations, we have used the P -statistic (Downes et al. 1986) which calculates the probability that a radio source of a given observed flux density could lie at the observed distance from the AzTEC source by chance. Only possible radio counterparts with values of $P \leq 0.05$ are considered robust, and are listed in Table 1, together with their distance offsets and P -values.

Out of the 189 AzTEC source candidates, 77 (40 per cent) have robustly associated radio counterparts within the COSMOS radio catalogue, and out of these 77, 7 (10 per cent) have a double robust association. These percentages are lower than those of other SMG studies (~ 60 – 70 per cent; e.g. Ivison et al. 2007; Biggs et al. 2011) due to the large incompleteness at the 1.4-GHz catalogue limit (a 4σ cut threshold is used) and shallower nature of the 1.4-GHz COSMOS data. This is also the reason why some previously claimed associations (see Table 1) are not identified in this study, as they were based on lower threshold detections.

5.3 Multiwavelength photometry

Table 1 summarizes the photometry derived from the comparison with other submm- to radio-wavelength catalogues. The 1.4-GHz flux densities of the robustly associated counterparts are one to two orders of magnitude lower than the deboosted 1.1-mm flux densities, with the exception of a few marked extended sources (see below), suggesting the mm flux has a thermal origin rather than the hyperluminous synchrotron-dominated blank-field sources identified by the South Pole Telescope (Vieira et al. 2010) or the variable $S_{1.2\text{mm}} > 10$ mJy flat-spectrum quasars discovered in MAMBO fields (Voss et al. 2006). None of the bright $S_{1.1\text{mm}}(\text{db}) \gtrsim 8$ mJy AzTEC sources is associated with luminous X-ray objects either (Johnson et al., in preparation), suggesting that, at best, they might harbour weak active galactic nuclei (AGN) or be Compton-thick.

In thermal-dominated sources, the mm to radio flux density ratio can be exploited as a redshift indicator. It increases monotonically with redshift, with some degeneracy due to the variety of radio synchrotron slopes and mm dust-emissivity indices present in the interstellar medium of those local galaxies used to define the relationship (Carilli & Yun 1999, 2000). Additionally, there exists a level of degeneracy between the temperature of the dust generating the rest-frame FIR luminosity (and hence mm flux) and the redshift. Regardless, by adopting a library of local galaxy templates, and accepting the intrinsic dispersion in their spectral energy distributions (SEDs), the 1.4 GHz to 1.1 mm flux density ratio still provides a crude but useful estimation of the redshift (Carilli & Yun 2000; Rengarajan & Takeuchi 2001; Aretxaga et al. 2007). This indicator becomes relatively insensitive to redshifts beyond $z \sim 3$, as the 1.1-mm filter starts to sample the flattening of the SED towards the rest-frame FIR peak, whilst still providing a powerful discriminant between low-redshift ($z < 2$) and high-redshift ($z > 2$) objects.

Fig. 9 represents the colour–redshift diagram of 20 local galaxies used as templates in the derivations of photometric redshifts (Aretxaga et al. 2007) and the colours measured for the AzTEC

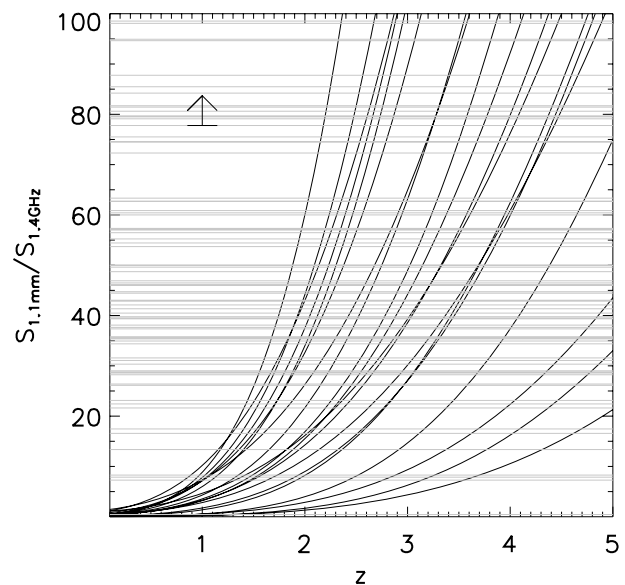


Figure 9. Millimetre to radio flux density ratio as a function of redshift for 20 local galaxies used as templates in the derivations of photometric redshifts of SMGs (Aretxaga et al. 2007). The grey horizontal lines represent the colours of the AzTEC galaxies with robustly associated radio counterparts, as in Table 1. The arrow at the top right corner represents the typical 3σ upper limit for SMGs in the COSMOS map with undetected radio counterparts.

sources with radio associations. Except for a few exceptions (such as AzTEC/C61, a likely radio-loud AGN, or C124 which is associated with a likely foreground radio galaxy at $z \sim 0.3$) that appear at the bottom of the diagram, the majority of the SMGs have mm-to-radio colours indicative of $z > 1$ systems, in accordance with the expectations derived from other (sub)mm-wavelength redshift distributions for the population (Aretxaga et al. 2003, 2007; Chapman et al. 2003, 2005; Pope et al. 2005; Valiante et al. 2007). A detail analysis of radio and optical–IR counterpart associations to these AzTEC sources and their inferred redshifts is deferred to an upcoming publication.

6 NUMBER COUNTS

We derive estimates for the number density of SMGs as a function of flux density, the so-called ‘number counts’ using the Bayesian technique originally outlined in Coppin et al. (2005, 2006) and used extensively in previous AzTEC publications (for example, see Austermann et al. 2009). While other techniques commonly used for the extraction of source counts from submm/mm-wavelength surveys, in particular the ‘ $P(D)$ ’ approach (e.g. Patanchon et al. 2009; Glenn et al. 2010), can in principle estimate the counts at fainter flux densities (i.e. below the detection limit of the survey), these methods are highly dependent on the assumed model, and the formally derived errors do not always represent the true uncertainty in the counts at faint flux densities (e.g. see discussions in Scott et al. 2010 and Glenn et al. 2010). On the other hand, with the Bayesian technique, the estimated counts are only weakly dependent on the assumed model of the prior distribution (Austermann et al. 2009, 2010), and the derived error bars more accurately describe the uncertainty in this estimate. For this reason, we use the Bayesian method, and derive the source counts only down to a flux density limit of $S(1.1 \text{ mm}) = 1.5 \text{ mJy}$.

We parametrize the number counts using a Schechter function:

$$\frac{dN}{dS} = N_{3 \text{ mJy}} \left(\frac{S}{3 \text{ mJy}} \right)^{\alpha+1} e^{-(S-3 \text{ mJy})/S'}, \quad (1)$$

with N being the number of sources per deg^2 , S being the source flux density at 1.1-mm wavelength, and α being the power-law slope of the faint-end counts. In this formalism, $N_{3 \text{ mJy}}$ has a natural interpretation as the number of sources per deg^2 with a flux of 3 mJy.

The measured flux densities of sources blindly detected in the AzTEC map must be corrected for biases resulting from the interaction between the Gaussian noise distribution in the map and the underlying flux density distribution of sources on the sky. We perform this correction by constructing the full posterior flux density distribution for each source, taking as a prior the parameters $N_{3 \text{ mJy}} = 160 \text{ deg}^{-2}$, $S' = 1.3 \text{ mJy}$ and $\alpha = -2.0$, which are consistent with those measured in the SHADES fields (Austermann et al. 2010). We nevertheless iterate on the adopted prior values to guarantee weak dependence on the starting values for the end results. For the $\geq 3.5\sigma$ peaks in the map, the full posterior probabilities are parametrized by their maxima and 68 per cent confidence levels, and are listed as deboosted fluxes in Table 1.

Once the full posterior flux distribution is derived for all $\geq 2.5\sigma$ peaks in the map, we cut all source candidates whose posterior flux distribution indicates a 5 per cent or greater probability of having a negative intrinsic flux. This is likely a very strict cut on our catalogue; however, the larger beam size and greater confusion in this survey warrant a conservative first approach (Austermann et al. 2009).

Table 2. COSMOS/ASTE differential and integral number counts, calculated as described in the text. The differential number counts flux bins are 1-mJy wide with effective bin centres (first column) weighted according to the assumed prior.

S (mJy)	dN/dS ($\text{mJy}^{-1} \text{ deg}^{-2}$)	S (mJy)	$N(> S)$ (deg^{-2})
1.41	394^{+116}_{-140}	1.00	1038^{+132}_{-157}
2.44	269^{+54}_{-60}	2.00	644^{+63}_{-70}
3.44	176^{+28}_{-31}	3.00	375^{+34}_{-38}
4.45	$99.5^{+15.0}_{-17.2}$	4.00	199^{+19}_{-22}
5.45	$49.9^{+8.9}_{-10.1}$	5.00	$99.1^{+11.3}_{-13.8}$
6.46	$22.3^{+5.0}_{-6.4}$	6.00	$49.1^{+7.0}_{-9.4}$
7.46	$10.3^{+3.4}_{-4.3}$	7.00	$26.9^{+4.8}_{-6.9}$
8.46	$5.83^{+2.33}_{-3.33}$	8.00	$16.63^{+3.47}_{-5.39}$
9.46	$4.07^{+1.80}_{-2.82}$	9.00	$10.79^{+2.57}_{-4.24}$
10.46	$2.94^{+1.40}_{-2.33}$	10.00	$6.72^{+1.83}_{-3.17}$
11.46	$1.87^{+0.87}_{-1.87}$	11.00	$3.78^{+1.18}_{-2.15}$

We bin our resulting catalogue in 1 mJy flux density bins, correct each bin for the corresponding completeness, and calculate dN/dS uncertainties by bootstrap sampling the dN/dS probability distribution in each bin 20 000 times, taking also into account the error in completeness. Table 2 lists the resulting bin centres, differential number counts and 68 per cent confidence interval uncertainties, and Fig. 10 shows the differential and integrated number counts derived for the full 0.72 deg^2 COSMOS field in this manner. Also plotted are the number counts for all other published AzTEC extragalactic blank fields (Perera et al. 2008; Scott et al. 2008; Austermann et al. 2010; Hatsukade et al. 2011) following a reanalysis of each of these maps using the same technique outlined in Section 3, in order to ensure that data processing effects take no role in the differences found.

Overall, the counts from different fields show some striking variance, especially if one focuses on the two largest, COSMOS and SHADES: the 0.72 deg^2 COSMOS field with systematically more sources at all flux levels than the 0.5 deg^2 (to approximately the same noise level) SHADES fields. The result, however, is not as extreme as that shown in the comparison with the smaller 0.15 deg^2 AzTEC/JCMT COSMOS field. In Sections 7 and 8, we will explore further these differences.

We derive best-fitting parameters for the Schechter function that describes the COSMOS/ASTE differential number counts by fitting equation (1) with a Levenberg–Marquardt least-squares algorithm that uses the full data–data covariance matrix in the χ^2 calculation. Our data do not meaningfully constrain the faint end of the counts and thus we fix the faint-end power-law index, α , to a value of -2 . This will also allow a direct comparison to similar fits in the literature. The best-fitting values of $N_{3 \text{ mJy}}$ and S' for COSMOS are given in Table 3, and Fig. 11 represents the error contours for these parameters.

7 AZTEC SOURCES VERSUS LARGE-SCALE STRUCTURE IN THE COSMOS FIELD

With the detection of ultrabright SMGs by AzTEC (Wilson et al. 2008b; Ikarashi et al. 2011), MAMBO (Lestrade et al. 2010), the South Pole Telescope (Vieira et al. 2010) and the *Herschel* satellite

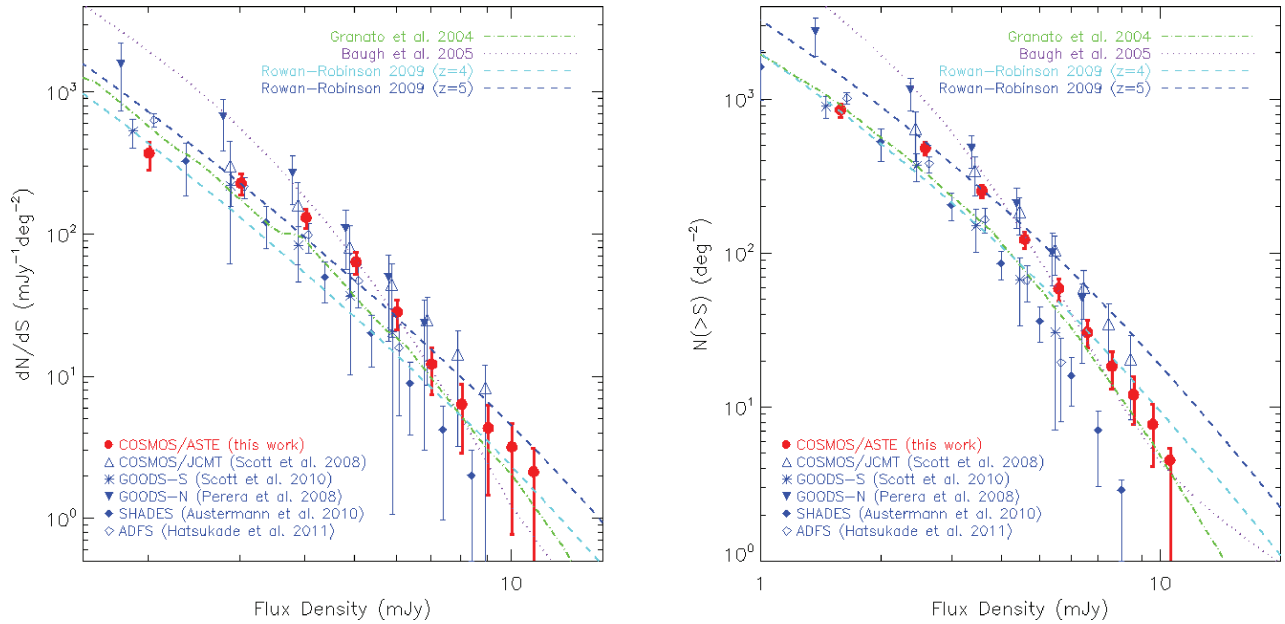


Figure 10. Left: differential number counts for the COSMOS AzTEC/ASTE field (red) along with the reanalysed counts from previously published AzTEC studies. Because of its large field, the COSMOS AzTEC/ASTE counts are more sensitive than previous studies in the 3–15 mJy range. Overplotted (lines) are a number of 1.1 mm number count predictions from an array of models for galaxy formation, where z for the Rowan-Robinson (2009) models denotes the free parameter that describes the onset of the IR-luminous phase. Right: corresponding integrated number counts at 1.1 mm.

Table 3. Best-fitting Schechter function parameters to the COSMOS AzTEC/ASTE differential number counts with α fixed to -2 .

$N_{3\text{mJy}}$ (deg^{-2})	S' (mJy)	α
207^{+18}_{-20}	2.25 ± 0.20	-2

(Negrello et al. 2010), there has been new attention given to the role that lensing plays in our view of the SMG population. Our AzTEC survey of the COSMOS field offers a prime opportunity to inspect the relationship between the background SMGs and the foreground large-scale structure mapped out at optical–IR wavelengths over a large redshift span. Indeed, with the 0.15 deg^2 AzTEC/JCMT map of COSMOS Austermann et al. (2009) already found a significant spatial correlation between the projected foreground ($z \lesssim 1$) galaxy population and the 50 SMG candidates. In this section we will take advantage of a much wider range of foreground large-scale structures covered within the 0.72 deg^2 AzTEC/ASTE map of COSMOS in order to test if the foreground structure significantly impacts our view of the blank-field SMG population and whether this might be the likely origin of the difference in number counts between COSMOS and SHADES.

Fig. 12 shows the projected density of optical–IR galaxies in the AzTEC field with photometric redshift $z_{\text{phot}} \leq 1.1$ along with the location of the 129 AzTEC sources with $S/N \geq 4.0$, $\lesssim 2$ per cent of which we expect to be spurious detections. While there is no apparent correlation between the positions of both populations, we can quantify this impression by comparing the distribution of projected densities of optical–IR galaxies within 30 arcsec radii circles centred on the AzTEC positions with those of 30 arcsec radii circles centred on random locations in the map (as in Austermann et al. 2009). A Kolmogorov–Smirnov (KS) D -test can then be used to

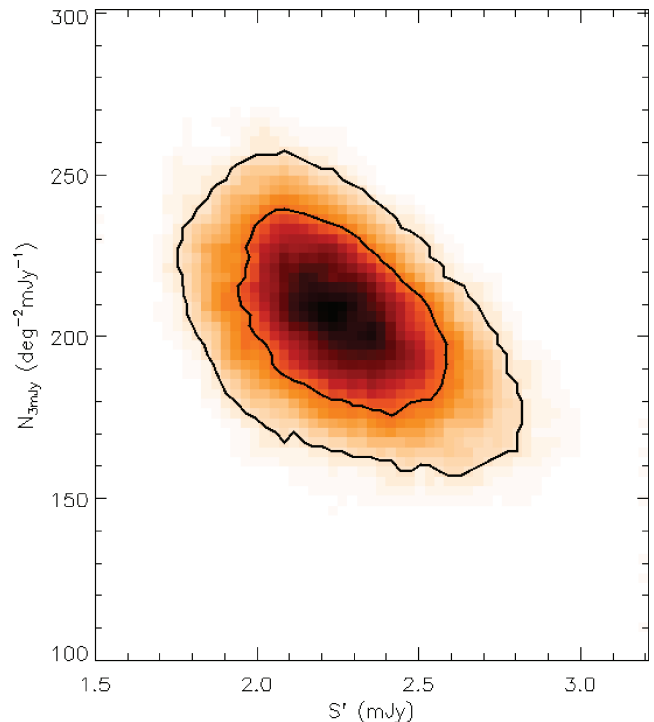


Figure 11. Confidence limits for $N_{3\text{mJy}}$ and S' when holding $\alpha = -2$. Contours represent the 68 and 95 per cent confidence limits.

ask with what probability we can rule out the null hypothesis that the two samples are drawn from the same parent distribution. As expected, the result, $P_{\text{KS}} = 68$ per cent, is consistent with no strong correlation between the optical–IR population at $z \leq 1.1$ and the $S/N \geq 4$ AzTEC catalogue.

Performing the same test with a flux cut on the AzTEC catalogue results in a more significant correlation detection. Considering only

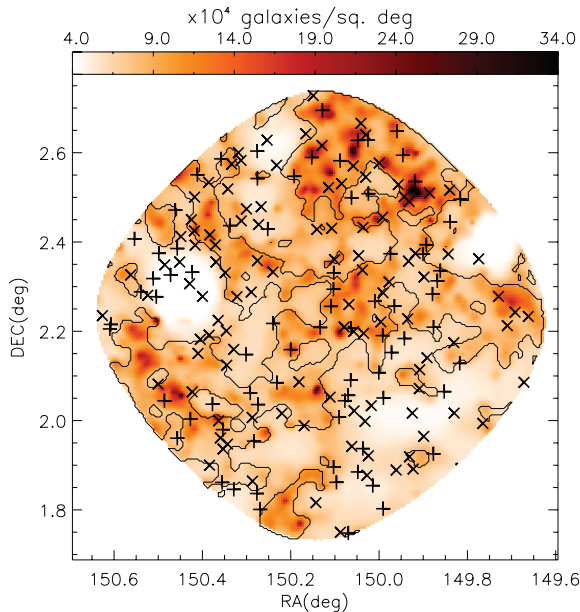


Figure 12. Smoothed surface density map of galaxies with photometric redshifts $z < 1.1$ derived from the optical–IR catalogue of COSMOS (Scoville et al. 2007b), updated to include photometric redshifts derived from 30 optical–IR bands (Ilbert et al. 2009). Only the 0.72 deg^2 area surveyed by AzTEC with uniform (≥ 50 per cent) coverage is represented. Darker colours indicate more densely populated areas of the sky. The cross and plus symbols represent AzTEC sources detected at $S/N \geq 4$ and $4 > S/N \geq 3.5$, respectively. The contours divide the map into zones with lower or higher than the average density of optical–IR galaxies. The total areas of these zones are 0.392 and 0.329 deg^2 , respectively.

the 41 $S/N \geq 5$ sources we find $P_{KS} = 1.8$ per cent, which is tentative evidence (at $\approx 2.4\sigma$ level) that the null hypothesis of no correlation is rejected. Indeed, for the 20 AzTEC sources with deboosted flux densities $S_{1.1\text{mm}} \geq 6 \text{ mJy}$, we can strongly reject the null hypothesis of identity between the distributions of galaxy densities around random positions in the AzTEC coverage area of the COSMOS field and galaxy densities around bright AzTEC sources: $P_{KS} = 0.11$ per cent ($\approx 3.3\sigma$).

The latest release of photometric redshifts for optical–IR-selected galaxies in the COSMOS field has achieved accuracies $\Delta z/(1+z) \approx 0.007$ to 0.012 at $z \lesssim 1.25$ (Ilbert et al. 2009). This statistical precision allows for the identification of large-scale structure pertaining to different redshift slices (see for example Scoville et al. 2007b). With this information in hand, we can search in redshift space for the structures that are more likely associated with the bright AzTEC sources. We will again compare the distributions of galaxy densities around AzTEC sources and around random positions in the AzTEC-covered COSMOS area at the redshift of interest. As a reference, if we take into account the AzTEC catalogue of 129 $S/N \geq 4$ sources, there is no significant signal of statistical differences between the distributions at any redshift (see Fig. 13).

However, if we restrict the analysis to the 20 sources with deboosted flux densities $S_{1.1\text{mm}} \geq 6 \text{ mJy}$, we identify the redshift ranges $0.58 \lesssim z \lesssim 0.76$ and $0.21 \lesssim z \lesssim 0.26$ as the ones in which most significant ($\sim 3\sigma$) differences are found between the median density of galaxies around AzTEC sources and the median density of galaxies around random positions (Fig. 13). The same redshift bins are highlighted if the analysis focuses on the 42 sources with deboosted flux densities $S_{1.1\text{mm}} \geq 5 \text{ mJy}$, although the probability of rejecting

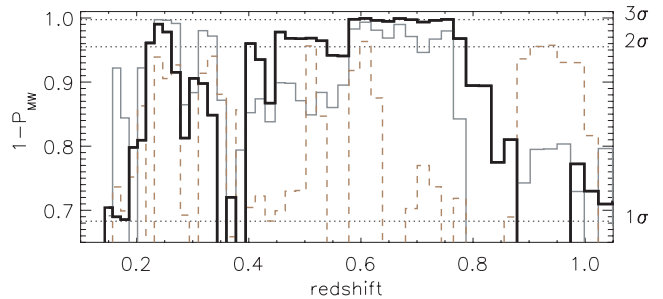


Figure 13. Probability that the median galaxy density around AzTEC sources is significantly larger than the density of galaxies around random positions in the AzTEC-covered map versus redshift. The thick black solid line represents probabilities around deboosted $S_{1.1\text{mm}} \geq 6 \text{ mJy}$ sources, the grey solid line represents probabilities around deboosted $S_{1.1\text{mm}} \geq 5 \text{ mJy}$ sources, and the dashed brown line represents probabilities around $S/N \geq 4$ sources. The redshift bins have an increasing step ranging from $\Delta z = 0.014$ to 0.026 , at $z = 0.15$ to 1.1 , to accommodate a sufficient sample of galaxies and the increasing degradation in photometric redshift precision (e.g. Scoville et al. 2007b).

the null hypothesis for the former redshift interval is smaller than for the latter.

The optical–IR galaxy density in these redshifts slices and the positioning of the bright AzTEC sources can be seen in Figs 14 and 15. In the interval $0.58 \lesssim z \lesssim 0.76$ we find that $S_{1.1\text{mm}} \geq 6 \text{ mJy}$ AzTEC sources have a significantly denser galaxy environment than that found at random positions in the map: the null hypothesis of identity between the medians of the distributions can be rejected at a $1 - P_{MW} = 99.88$ per cent confidence level, while for $S_{1.1\text{mm}} \geq 5 \text{ mJy}$ AzTEC sources that level gets reduced to $1 - P_{MW} = 98.7$ per cent. In the interval $0.21 \lesssim z \lesssim 0.26$ the reverse happens, finding that the $S_{1.1\text{mm}} \geq 6 \text{ mJy}$ AzTEC sources have a denser environment with a significance $1 - P_{MW} = 99.2$ per cent. The significance gets increased to $1 - P_{MW} = 99.95$ per cent if $S_{1.1\text{mm}} \geq 5 \text{ mJy}$ sources are considered. The effect seems to be carried by four $5 \leq S_{1.1\text{mm}} < 6 \text{ mJy}$ sources that coincide with large density peaks, rather than by the general population of intermediate/brightness sources, though. If one excludes the $S_{1.1\text{mm}} \geq 6 \text{ mJy}$ sources from the analysis, the probability drops to $1 - P_{MW} = 99.0$ per cent.

These two redshift intervals are the same ones we identified as having the largest correlation between $z \lesssim 1.1$ optical–IR galaxies and AzTEC sources for the smaller 0.15 deg^2 field observed by AzTEC in the JCMT (Austermann et al. 2009). It is thus important to know if the correlations arise mainly due to the very rich clusters located in the area of the sky previously sampled, or if this is a trend observed over the larger 0.72 deg^2 field, which might be more representative of a generic blank field.

In Austermann et al. (2009) we showed that the association of bright AzTEC sources around areas of large galaxy densities was not exclusively due to the presence of massive rich clusters. If we mask out the areas marked as #1 and #24 in Fig. 14, which represent the FWHM of the two massive clusters at $0.58 \lesssim z \lesssim 0.76$ identified in the large-scale structure analysis of Scoville et al. (2007b), and exclude the sources that fall within those areas, the probability of having a median of galaxy densities around AzTEC sources larger than that of random positions by chance is only $P_{MW} = 0.3$ per cent. The distributions are shown in Fig. 16. Likewise, if we exclude from the correlation analysis the overlapping area common to the AzTEC/JCMT and AzTEC/ASTE maps (encircled in dashed blue lines in Figs 14 and 15), the remaining 12 $S_{1.1\text{mm}} \geq 6 \text{ mJy}$ sources still show a larger tendency of falling within the large galaxy-density

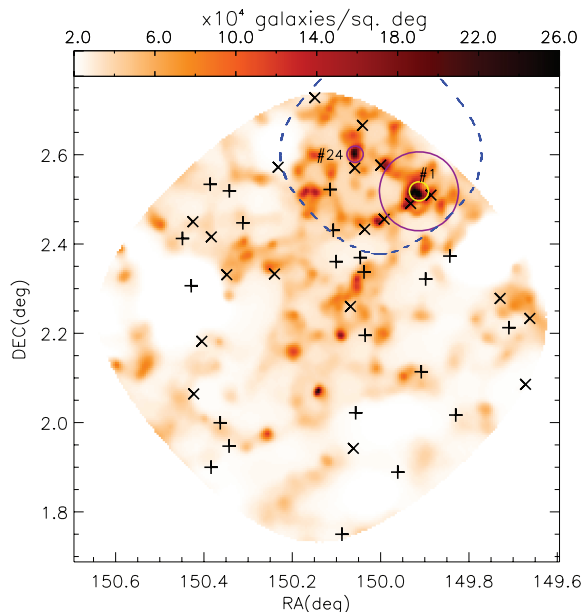


Figure 14. Smoothed surface density map of galaxies at $0.58 \lesssim z \lesssim 0.76$ detected at optical-IR wavelengths by the COSMOS survey within the uniform coverage area of the AzTEC/ASTE map. The cross symbols represent 20 AzTEC sources detected with deboosted flux densities $S_{1.1\text{mm}} \geq 6$ mJy. The plus symbols denote sources detected with deboosted flux densities $5 \leq S_{1.1\text{mm}} < 6$ mJy. A massive cluster at $z \approx 0.73$ (Guzzo et al. 2007) located in the north-west of the map is marked as #1. The inner yellow circle of 1.5 arcmin diameter marks the core of X-ray emission, while the purple 6 arcmin diameter circle marks the FWHM of the optical/IR overdensity associated with the cluster (Scoville et al. 2007b). Another rich cluster at $z \approx 0.61$ from the large-scale structure catalogue of COSMOS (Scoville et al. 2007b) is marked as #24, and the FWHM of the optical/IR overdensity is encircled in purple. The outer blue dashed line contour depicts the edge of the uniform coverage of the AzTEC map observed in 2005 at the JCMT (Scott et al. 2008).

regions mapped at optical-IR wavelengths at $z \lesssim 1.1$. In that case, the null hypothesis of identity between the medians of the distributions can be rejected at a $1 - P_{\text{MW}} = 97.0$ per cent confidence level.

8 DISCUSSION

8.1 Effects of foreground structure on number counts

With evidence that our detected SMGs are spatially correlated with foreground ($z \leq 1.1$) large-scale structure in the COSMOS field, we now ask what effect, if any, this structure might have on our estimation of the SMG number counts. We address this by first dividing the catalogue into two subsamples: SMGs that lie in regions of the map with foreground galaxy densities larger than the average density of the field and SMGs that lie in regions with foreground galaxy densities smaller than the average galaxy density of the field. Fig. 12 shows the two regions along with the respective locations of the corresponding SMGs.

Fig. 17 shows the number counts resulting from splitting sources in high and low foreground galaxy-density environments. While none of the dN/dS bins individually show a clear, statistically significant deviation from the mean counts over the field, the data clearly suggest that, consistent with the results of Section 7, at high fluxes ($S_{1.1\text{mm}} \geq 6$ mJy) the counts are systematically higher for

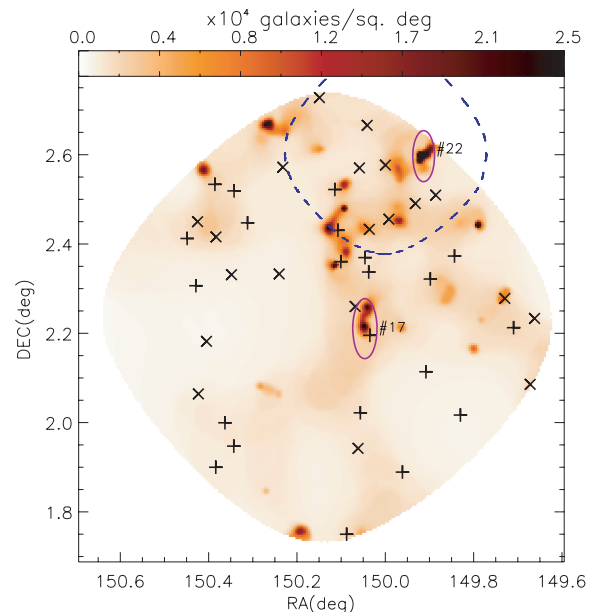


Figure 15. Smoothed surface density map of galaxies at $0.21 \lesssim z \lesssim 0.26$ detected at optical-IR wavelengths by the COSMOS survey within the uniform coverage area of the AzTEC map observed in 2008. Symbols and lines are as in Fig. 14. Two rich clusters from the catalogue of large-scale structures in COSMOS (Scoville et al. 2007b) are marked as #17 and #22.

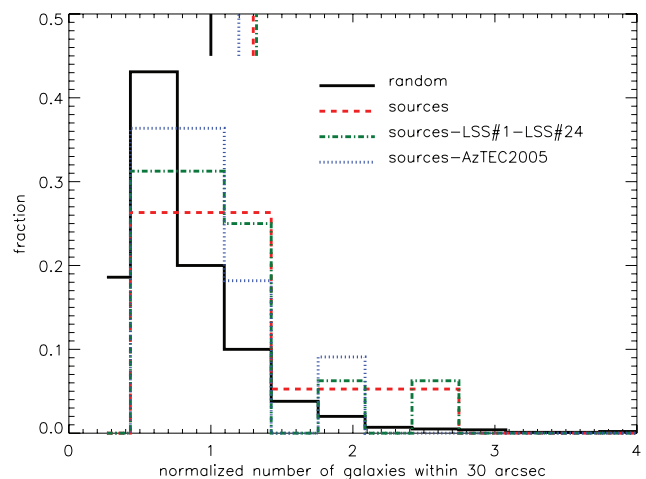


Figure 16. Histograms of the number of optical/IR galaxies around random positions in the AzTEC-covered COSMOS map, normalized to the mean value over the whole map, represented by a solid black line. The dashed, dash-dot-dash and dot-dashed lines represent the distribution of number of galaxies found around AzTEC sources with deboosted flux densities $S_{1.1\text{mm}} \geq 6$ mJy in the entire AzTEC-covered COSMOS map, excluding the 6 arcmin diameter area around clusters #1 and #24, and excluding the whole uniform area mapped by AzTEC in 2005 in the JCMT. The vertical bars at the top of the diagram mark the mean values of the distributions.

the high foreground galaxy-density sample. This result can also be made evident by representing the distribution of flux densities of the SMGs that fall within the low and high galaxy-density areas of the map (see Fig. 18). The null hypothesis that the 1.1 mm flux density distribution of sources that fall within low- and high-density areas are similar can be rejected, as differences as large as the one measured can only be produced by chance in 0.37 per cent of situations.

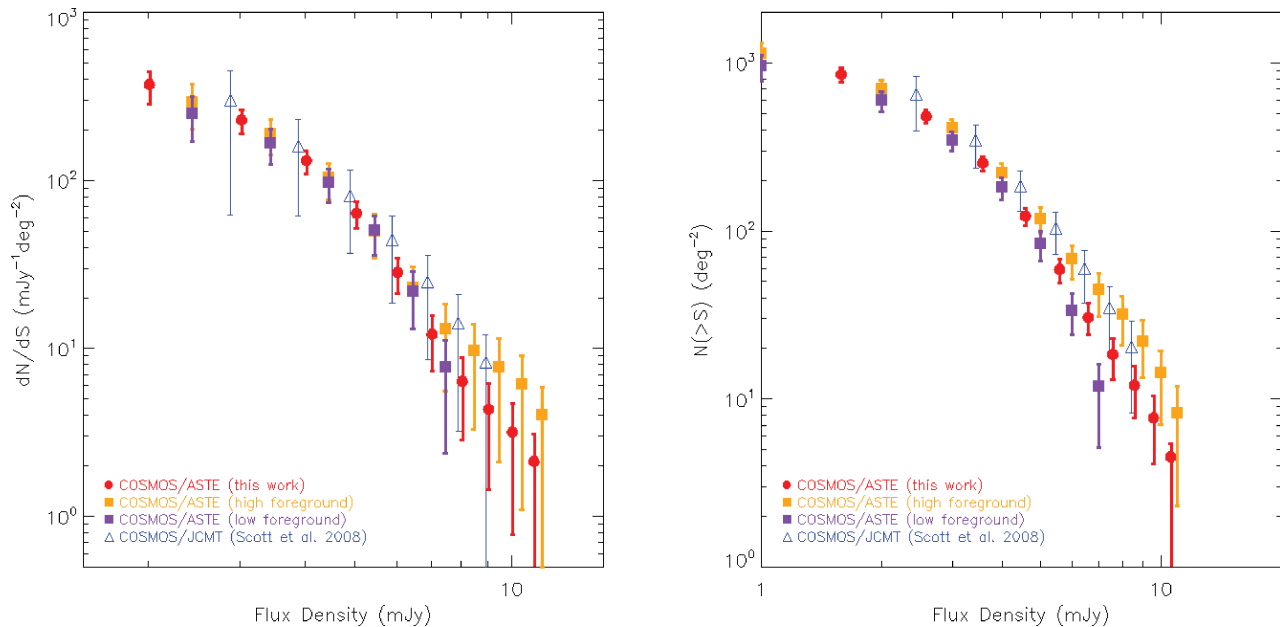


Figure 17. Left: differential number counts derived for regions of low and high galaxy density within the AzTEC/ASTE-covered COSMOS area. ‘High foreground’ denotes sources that fall in regions of the map with greater than the mean foreground galaxy density. ‘Low foreground’ denotes sources that fall in regions of the map with less than the mean foreground galaxy density. Triangles denote counts from the COSMOS/JCMT. Right: corresponding integral number counts.

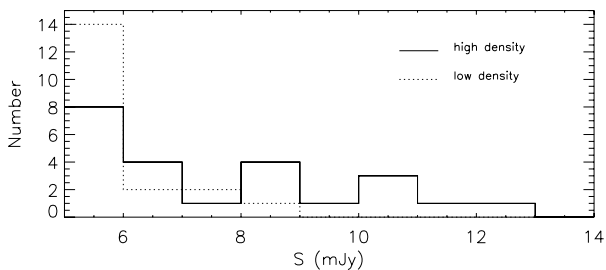


Figure 18. Distribution of fluxes for the 60 brightest ($S_{1.1\text{mm}} \geq 5$ mJy) AzTEC sources that fall within high galaxy-density areas (continuous line) and within low galaxy-density areas (dotted line) of the COSMOS map. The high-density areas host the majority of the brightest sources. The null hypothesis that the two distributions can be derived from the same parent distribution can be rejected with a probability $P_{KS} = 0.37$ per cent.

The number counts for the low-density galaxy sample are closer to the number counts derived for SHADES, if still systematically above them (by ~ 16 per cent in flux density), while the high-density galaxy sample aligns with the results derived for COSMOS/JCMT and GOODS-N (about ~ 30 – 40 per cent offset in flux density at $S_{1.1\text{mm}} \gtrsim 5$ mJy, compare with Fig. 10). It is thus apparent that an accurate description of the overall population will fall somewhere in between these solutions, and that despite having sampled 0.72 deg^2 in COSMOS and 0.5 deg^2 in SHADES at comparable noise levels, this is not yet a large enough area to avoid variance due to intrinsic clustering of the SMG population and amplification by foreground structures.

The optical–IR galaxies that compose the COSMOS galaxy-density map have accurate photometric redshifts that place them at $z \leq 1.1$, while most of the redshifts of the SMGs uncovered by AzTEC are still unknown. Furthermore, the largest amplitude correlation between the positions of optical–IR galaxies and SMGs occurs at $0.6 \lesssim z \lesssim 0.75$ (Section 7), where only a ~ 3 per cent

of $850\text{-}\mu\text{m}$ SMGs with radio associations are statistically located (Chapman et al. 2005). Photometric arguments (Fig. 9, Section 5.3) place the majority of AzTEC SMGs at $z \gtrsim 1$ (see also Younger et al. 2007, 2009), and the four bright targets with refined interferometric positions by SMA that have been spectroscopically targeted and have robust redshifts are indeed at $z > 1.1$ (Table 1; Riechers et al. 2010; Capak et al. 2011, in preparation; Smolčić et al. 2011). While there is no proof that all bright $S_{1.1\text{mm}} \geq 6$ mJy sources are at high redshifts, it is likely that most of these sources are at $z > 1$ and that their association with the optical–IR galaxy large-scale structure is through amplification, an explanation already posed to account for the discrepancies between the number counts measured in the smaller COSMOS AzTEC/JCMT field and SHADES (Austermann et al. 2009). Our new results, thus, confirm this interpretation for a more representative area of the sky that is not dominated by the presence of a rich cluster environment.

Lensing of galaxies by foreground galaxies and by foreground groups of galaxies has been shown to be the reason for the presence of a very bright (sub)mm-selected galaxy population (Lestrade et al. 2010; Negrello et al. 2010; Vieira et al. 2010; Ikarashi et al. 2011). These galaxies are extreme cases of the phenomena presented here, where moderate ~ 20 per cent amplification factors would be enough to account for the flux density offset between the number counts of SHADES and COSMOS.

Light propagation experiments in cosmological simulations using multiple lens-plane algorithms show that at $z > 1$ any population is subject to a large chance of amplification by foreground structures (e.g. Martel & Premadi 2008). Correlations between bright SMGs and foreground optically selected galaxies at $z \sim 0.5$ were first detected using a small sample of $S_{850\text{ }\mu\text{m}} \gtrsim 8$ mJy sources in the UK 8-mJy survey and *Hubble Deep Field* (Almaini et al. 2005). The analysis of a statistically robust sample of 2477 $350\text{-}\mu\text{m}$ -selected SMGs in the Lockman-SWIRE field, which includes the smaller UK 8-mJy survey area studied previously, has confirmed correlations

between the SMG population and $z \sim 0.2$ and 0.4 optical and IR-selected galaxy samples (Wang et al. 2011). Our first 0.15 deg^2 survey in the COSMOS field scanned all foreground structures at $0 < z < 1$, yielding significant correlations between the bright 1.1-mm -selected SMGs detected in the field and optical–IR galaxies at redshifts $z \sim 0.25$ and 0.65 (Austermann et al. 2009). Whether these correlations were dominated by the optical–IR overdensity of galaxies where the AzTEC survey had been acquired or inherent of amplifications to the general blank-field population was open to debate. Our new analysis in COSMOS allows for a better estimation of the structures that contribute to the possible boosting of flux densities of SMGs by foreground structures, identifying the $0.21 \lesssim z \lesssim 0.26$ and, most significantly, the $0.58 \lesssim z \lesssim 0.76$ redshift bins as those with the largest probability of association with bright $S_{1.1 \text{ mm}} \gtrsim 5 \text{ mJy}$ sources. The first redshift interval is common to the $350\text{-}\mu\text{m}$ -selected SMG correlations result. The second redshift interval, however, is still unexplored by other experiments.

Other populations of high- z galaxies also should show similar amplification trends. The positions of bright Lyman-break galaxies selected to be at $z \approx 2.5$ to 5 in the Canada–France–Hawaii Telescope Legacy Survey are, indeed, positively correlated with optically selected galaxies at $z < 1.4$, and this effect has been shown to be consistent with weak lensing by the foreground structures in the line of sight (Hildebrandt, van Waerbeke & Erben 2009). Strong lensing is also predicted to be a dominating effect in the bright number counts of SMGs (Blain 1996; Negrello et al. 2007; Lima, Jain & Devlin 2010); however, neither strong nor weak lensing is often included in the predictions of observables offered by galaxy formation models.

8.2 Comparison with galaxy formation models

Fig. 10 shows the number counts of COSMOS compared with several galaxy formation models that have successfully reproduced overall properties of the SMG and SMG population (Granato et al. 2004; Baugh et al. 2005; Rowan-Robinson 2009). The 1.1 mm number counts of the SHADES field were compared with these very same models (Austermann et al. 2010), and it was found that they all overpredicted the number counts in the $\gtrsim 3 \text{ mJy}$ regime. The discrepancies with the new 0.72 deg^2 AzTEC/ASTE COSMOS field are not that severe. While the Granato et al. (2004) model for the joint formation of quasi-stellar objects and SMGs could be made compatible with the COSMOS number counts using a small shift in flux density that would mimic the amplification claimed in this paper, the model overpredicts the $S_{1.1 \text{ mm}} \lesssim 2 \text{ mJy}$ number counts, which, although poorly constrained by the COSMOS data alone, have more robust estimations from smaller deeper fields (Scott et al. 2010; Hatsukade et al. 2011). The Baugh et al. (2005) model offers a good description of the COSMOS number counts at $S_{1.1 \text{ mm}} \gtrsim 4 \text{ mJy}$, but it overpredicts the number counts at lower flux densities, while the Rowan-Robinson (2009) models have a different functional form to that found for COSMOS over the whole flux density range sampled by our study.

9 CONCLUSIONS

The number counts of the COSMOS 0.72 deg^2 AzTEC/ASTE field show an overdensity of sources with respect to the population of SMGs found in previous large blank-field surveys such as SHADES (Austermann et al. 2010). The number counts derived for the COSMOS field display a systematic positive offset over those of SHADES, but are nevertheless consistent with those derived from

smaller fields that were considered too small to characterize the overall blank-field population. We identify departures to occur more significantly in the $S_{1.1 \text{ mm}} \gtrsim 5 \text{ mJy}$ regime, and demonstrate that these differences are related to the areas where galaxies at redshifts $z \lesssim 1.1$ are more densely clustered. The positions of optical–IR galaxies in the redshift interval $0.60 \lesssim z \lesssim 0.75$ are the most strongly correlated with the positions of the 1.1-mm bright population ($S_{1.1 \text{ mm}} \geq 6 \text{ mJy}$), a result which does not depend exclusively on the presence of rich clusters within the survey sampled area. The most likely cause of these departures in number counts at 1.1 mm is lensing by either foreground galaxies or foreground groups of galaxies at moderate amplification levels, which increases in amplitude as one samples larger and larger flux densities. Our results and the comparison with the previously published SHADES number counts illustrate the fact that even $\sim 0.70 \text{ deg}^2$ surveys are still subject to variance due to the small volume sampled by the mapped areas in conjunction to the chance amplification by foreground structures.

ACKNOWLEDGMENTS

This work has been supported in part by Conacyt (Mexico) grants 39953-F and 39548-F, NSF (USA) grants AST-0907952 and AST-0838222, and by the MEXT Grant-in-Aid for Specially Promoted Research (No. 20001003). Observations with ASTE carried out remotely from Japan used NNT’s GEMnet2 and its partner R&E networks, which are based on the AccessNova collaboration of the University of Chile, NTT Laboratories and the NOAJ. We would like to thank everyone who supported the AzTEC/ASTE observations of the COSMOS field, including E. Akiyama, R. Cybulski, K. Fukue, S. Harasawa, S. Ikarashi, H. Inoue, M. Kawamura, A. Kuboi, J. Rand, M. Tashiro, T. Tosaki, T. Tsukagoshi, Y. Shimajiri and C. Williams. The ASTE project is driven by the Nobeyama Radio Observatory (NRO), a branch of the National Astronomical Observatory of Japan (NAOJ), in collaboration with the University of Chile and Japanese institutions including the University of Tokyo, Nagoya University, Osaka Prefecture University, Ibaraki University and Hokkaido University.

REFERENCES

- Aguirre J., Bolocam – COSMOS Collaboration, 2006, American Astron. Soc. Meeting, 209, 8004
 Almaini O., Dunlop J. S., Willot C. J., Alexander D. M., Bauer F. E., Liu C. T., 2005, MNRAS, 358, 875
 Aretxaga I., Hughes D. H., Chapin E. L., Gaztanaga E., Dunlop J. S., Ivison R. J., 2003, MNRAS, 342, 759
 Aretxaga I. et al., 2007, MNRAS, 379, 1571
 Austermann J. et al., 2009, MNRAS, 393, 1573
 Austermann J. et al., 2010, MNRAS, 401, 160
 Barger A. J., Cowie L. L., Sanders D. B., Fulton E., Taniguchi Y., Sato Y., Kawara K., Okuda H., 1998, Nat, 394, 248
 Baugh C. M., Lacey C. G., Frenk C. S., Granato G. L., Silva L., Bressan A., Benson A. J., Cole S., 2005, MNRAS, 356, 1191
 Bertoldi F. et al., 2007, ApJS, 172, 132
 Biggs A. D. et al., 2011, MNRAS, 412, 2314
 Blain A. W., 1996, MNRAS, 283, 1240
 Capak P. L. et al., 2011, Nat, 470, 233
 Carilli C., Yun M. S., 1999, ApJ, 513, 13
 Carilli C., Yun M. S., 2000, ApJ, 530, 618
 Chapman S. C., Blain A. W., Ivison R. J., Smail I. R., 2003, Nat, 422, 695
 Chapman S. C., Blain A. W., Smail I. R., Ivison R. J., 2005, ApJ, 622, 772
 Condon J. J., 1992, ARA&A, 30, 575
 Coppin, Halpern H., Scott D., Borys C., Chapman S., 2005, MNRAS, 357, 1022

- Coppin K., 2006, MNRAS, 372, 1621
Downes A. J. B., Peacock J. A., Savage S., Carrie D. R., 1986, MNRAS, 218, 31
Downes T. P., Welch D. E., Scott K., Austermann J., Wilson G. W., 2011, MNRAS, submitted, preprint (arXiv:1103.3072)
Dye S. et al., 2008, MNRAS, 386, 1107
Ezawa H., Kawabe R., Kohno K., Yamamoto S., 2004, in Oschmann J. M., Jr, ed., Proc. SPIE Vol. 5489, Ground-based Telescopes. SPIE, Bellingham, p. 763
Ezawa H. et al., 2008, in Stepp L. M., Gilmozzi R., eds, Proc. SPIE Vol. 7012, Ground-based and Airborne Telescopes II. SPIE, Bellingham, 701208
Glenn J. et al., 2010, MNRAS, 409, 109
Granato G. L., De Zotti G., Silva L., Bressan A., Danese L., 2004, ApJ, 600, 580
Greve T. R. et al., 2005, MNRAS, 359, 1165
Griffin M. J., Orton G. S., 1993, Icarus, 105, 537
Guzzo L. et al., 2007, ApJS, 172, 254
Hatsukade B. et al., 2011, MNRAS, 411, 102
Helou G., Soifer B. T., Rowan-Robinson M., 1985, ApJ, 298, 7
Hildebrandt H., van Waerbeke L., Erben T., 2009, A&A, 507, 683
Hughes D. H. et al., 1998, Nat, 394, 241
Ikarashi S. et al., 2011, MNRAS, in press, preprint (arXiv1009.1455)
Ilbert O. et al., 2009, ApJ, 690, 1236
Iverson R. et al., 2002, MNRAS, 337, 1
Iverson R. et al., 2007, MNRAS, 380, 199
Kamazaki T. et al., 2005, in Schopbell P., Britton H., Ebert R., eds, ASP Conf. Ser. Vol. 347, Astronomical Data Analysis Software and Systems. Astron. Soc. Pac., San Francisco, p. 533
Laurent G. T. et al., 2005, ApJ, 623, 742
Lestrade J.-F., Combes F., Salome P., Omont A., Bertoldi F., Andre P., Schneider N., 2010, A&A, 522, L4
Lima M., Jain B., Devlin M., 2010, MNRAS, 406, 2352
Martel H., Premadi P., 2008, ApJ, 673, 657
Negrello M., Perrotta F., González-Nuevo González J., Silva L., De Zotti G., Granato G. L., Baccigalupi C., Danese L., 2007, MNRAS, 377, 1557
Negrello M. et al., 2010, Sci, 330, 800
Patanchon G. et al., 2009, ApJ, 707, 175
Perera T. et al., 2008, MNRAS, 391, 1227
Pope A., Borys C., Scott D., Conselice C., Dickinson M., Mobasher B., 2005, MNRAS, 358, 149
Rengarajan T. N., Takeuchi T. T., 2001, PASJ, 53, 433
Riechers D. A. et al., 2010, ApJ, 720, 131
Rowan-Robinson M., 2009, MNRAS, 394, 117
Schinnerer E. et al., 2010, ApJS, 188, 384
Scott K. et al., 2008, MNRAS, 385, 2225
Scott K. et al., 2010, MNRAS, 405, 2260
Scoville N. et al., 2007a, ApJS, 172, 1
Scoville N. et al., 2007b, ApJS, 172, 150
Smail I., Iverson R. J., Blain A. W., 1997, ApJ, 490, L5
Smolčić V. et al., 2011, ApJ, 731, L27
Tacconi L. J. et al., 2008, ApJ, 680, 246
Valiante E., Lutz D., Sturm E., Genzel R., Tacconi L. J., Lehnert M. D., Baker, A. J., 2007, ApJ, 660, 1060
Vieira J. et al., 2010, ApJ, 719, 763
Voss H., Bertoldi F., Carilli C., Owen F. N., Lutz D., Holdaway M., Ledlow M., Menten K. M., 2006, A&A, 448, 823
Wang L. et al., 2011, MNRAS, in press
Weiß A. et al., 2009, ApJ, 707, 1201
Wilson G. W. et al., 2008a, MNRAS, 386, 807
Wilson G. W. et al., 2008b, MNRAS, 390, 1061
Younger et al., 2007, ApJ, 671, 1531
Younger et al., 2009, ApJ, 704, 803
Yun M. S., Reddy N. A., Condon J. J., 2001, ApJ, 554, 803

This paper has been typeset from a $\text{\TeX}/\text{\LaTeX}$ file prepared by the author.